Mineralogical Magazine (2019), **83**, 293–313
doi:10.1180/mgm.2018.125

CAMBRIDGE UNIVERSITY PRESS

New minerals tsangpoite $Ca_5(PO_4)_2(SiO_4)$ and matyhite $Ca_9(Ca_{0.5}\square_{0.5})Fe(PO_4)_7$ from the D'Orbigny angrite

Shyh-Lung Hwang[1]*, Pouyan Shen[2], Hao-Tsu Chu[3], Tzen-Fu Yui[4], Maria-Euginia Varela[5] and Yoshiyuki Iizuka[4]

[1]Department of Materials Science and Engineering, National Dong Hwa University, Hualien, Taiwan, ROC; [2]Department of Materials Science and Optoelectronic Science, National Sun Yat-sen University, Kaohsiung, Taiwan, ROC; [3]Central Geological Survey, PO Box 968, Taipei, Taiwan, ROC; [4]Institute of Earth Sciences, Academia Sinica, Taipei, Taiwan, ROC; and [5]Instituto de Ciencias Astronómicas de la Tierra y del Espacio (ICATE) Avenida España 1512 sur, J5402DSP, San Juan, Argentina

Abstract

Tsangpoite, ideally $Ca_5(PO_4)_2(SiO_4)$, the hexagonal polymorph of silicocarnotite, and matyhite, ideally $Ca_9(Ca_{0.5}\square_{0.5})Fe(PO_4)_7$, the Fe-analogue of Ca-merrillite, were identified from the D'Orbigny angrite meteorite by electron probe microanalysis, electron microscopy and micro-Raman spectroscopy. On the basis of electron diffraction, the symmetry of tsangpoite was shown to be hexagonal, $P6_3/m$ or $P6_3$, with $a = 9.489(4)$ Å, $c = 6.991(6)$ Å, $V = 545.1(6)$ Å^3 and $Z = 2$ for 12 oxygen atoms per formula unit, and that of matyhite was shown to be trigonal, $R3c$, with $a = 10.456$ (7) Å, $c = 37.408(34)$ Å, $V = 3541.6$ (4.8) Å^3 and $Z = 6$ for 28 oxygen atoms per formula unit. On the basis of their constant association with the grain-boundary assemblage: Fe sulfide + ulvöspinel + Al–Ti-bearing hedenbergite + fayalite–kirschsteinite intergrowth, the formation of tsangpoite and matyhite, along with kuratite (the Fe-analogue of rhönite), can be readily rationalised as crystallisation from residue magmas at the final stage of the D'Orbigny meteorite formation. Alternatively, the close petrographic relations between tsangpoite/matyhite and the resorbed Fe sulfide rimmed by fayalite + kirschsteinite symplectite, such as the nucleation of tsangpoite in association with magnetite ± other phases within Fe sulfide and the common outward growth of needle-like tsangpoite or plate-like matyhite from the fayalite–kirschsteinite symplectic rim of Fe sulfide into hedenbergite, infer that these new minerals and the grain-boundary assemblage might represent metasomatic products resulting from reactions between an intruding metasomatic agent and the porous olivine–plagioclase plate + fayalite–kirschsteinite overgrowth + augite + Fe sulfide aggregates. Still further thermochemical and kinetics evidence is required to clarify the exact formation mechanisms/conditions of the euhedral tsangpoite, matyhite and kuratite at the grain boundary of the D'Orbigny angrite.

Keywords: angrite, D'Orbigny, new mineral, tsangpoite, matyhite

(Received 16 October 2017; accepted 9 April 2018)

Introduction

Tsangpoite, $Ca_5(PO_4)_2(SiO_4)$ ($P6_3$ or $P6_3/m$; $a = 9.489(4)$ Å, $c = 6.991(6)$ Å, $V = 545.1(6)$ Å^3 and $Z = 2$), the hexagonal polymorph of silicocarnotite, and matyhite, $Ca_9(Ca_{0.5}\square_{0.5})Fe(PO_4)_7$ ($R3c$, $a = 10.456(7)$ Å, $c = 37.408(34)$ Å, $V = 3541.6(4.8)$ Å^3 and $Z = 6$), the Fe-analogue of Ca-merrillite, were identified from the D'Orbigny angrite meteorite in this study. Angrites are a small group of achondritic meteorites of basaltic composition, and are generally believed to be formed by rapid crystallisation of unusual Ca-, Al-, Ti-rich and Na-, K-poor magmas at the very early stage of solar system history (Prinz *et al.*, 1977; Goodrich, 1988; McKay *et al.*, 1988, 1990; Mittlefehldt and Lindstrom, 1990; Prinz and Weisberg, 1995; Mikouchi *et al.*, 1996; Mikouchi and McKay, 2001; Mittlefehldt *et al.*, 2002; Keil, 2012). Angrites consist mainly of anorthite, olivine, Al–Ti augite and kirschsteinite, as well as grain-boundary phases such as Al–Ti-rich hedenbergite, Ca–Fe-rich olivine, Fe sulfide (FeS, troilite), ulvöspinel, and unusual minerals such as kuratite (the Fe-analogue of rhönite, IMA2013-109; described as Ti-silicate or rhönite in Mittlefehldt *et al.*, 2002; Kurat *et al.*, 2004; Jambon and Boudouma, 2011; Hwang *et al.*, 2016*a*), and some silico-phosphates with variable SiO_2, characteristically high FeO, and very low F and Cl contents (see table 8 in Keil, 2012).

Tsangpoite, referred to as a Ca silico-phosphate with ~10–15 wt.% SiO_2 and ~25–35wt.% P_2O_5 in Kaneda *et al.* (2001), was first reported in Asuka 881371 (Prinz and Weisberg, 1995; Warren and Davis, 1995), and later in other samples such as D'Orbigny (Kaneda *et al.*, 2001; Mittlefehldt *et al.*, 2002), NWA 1296 & 1670 (Jambon *et al.*, 2005; 2008) and NWA 4590 (Mikouchi *et al.*, 2011). However, due to the low abundance and small crystal size, as well as variable SiO_2 and FeO contents, determination of the stoichiometry of tsangpoite in most cases was inconclusive. It was noted that the compositions of tsangpoite are close to silicocarnotite or nagelschmidtite, but slightly different from both of them (e.g. Kaneda *et al.*, 2001; Mikouchi *et al.*, 2010). Structurally, the early synchrotron X-ray Laue pattern of tsangpoite from Asuka 881371 did not match that of merrillite, apatite, silicocarnotite or 'fassaite' (Kaneda *et al.*, 2001). Micro-Raman and electron back-scatter diffraction (EBSD) analyses using scanning electron microscopy (SEM), however, showed that the tsangpoite from D'Orbigny could be isostructural to apatite (Mikouchi *et al.*, 2010). This is further supported by X-ray diffraction (XRD) of the exceptionally large tsangpoite crystals (a few hundreds of μm) with a high $Fe^{3+}/\Sigma Fe$ ratio (~0.8; X-ray absorption near edge structure (XANES) analysis) showing an apatite-like unit cell and space group (Mikouchi *et al.*, 2011). Further, in this present investigation we show that tsangpoite, with a hexagonal structure, a silicocarnotite-like stoichiometry,

***Author for correspondence:** Shyh-Lung Hwang, Email: slhwang@gms.ndhu.edu.tw
Associate Editor: Sergey Krivovichev
Cite this article: Hwang S.-L., Shen P., Chu H.-T., Yui T.-F., Varela M.-E. and Iizuka Y. (2019) New minerals tsangpoite $Ca_5(PO_4)_2(SiO_4)$ and matyhite $Ca_9(Ca_{0.5}\square_{0.5})Fe(PO_4)_7$ from the D'Orbigny angrite. *Mineralogical Magazine* **83**, 293–313. https://doi.org/10.1180/mgm.2018.125

and abundant structure vacancies due to aliovalent cation substitution, is most probably structurally related to the α-Ca_2SiO_4 high-*T* polymorph, as are flamite, nagelschmidtite and silicocarnotite (Saalfeld and Klaska,1981; Gfeller *et al.*, 2015; Widmer *et al.*, 2015; Galuskin *et al.*, 2016). This indicates a mineralogical origin for tsangpoite at $T > 1200$°C, similar to the high-temperature hexagonal phase(s) in the α-Ca_2SiO_4–ᾱ-$Ca_3(PO_4)_2$ binary system, although an apatite-like structure with fully empty anion channels for tsangpoite cannot be excluded completely pending future single-crystal refinements. With the stoichiometry and structure unknown in other mineral species, tsangpoite should be considered as the first new mineral in the silicate–phosphate category in meteorites (Hwang *et al.*, 2015; Rubin and Ma, 2017).

Matyhite, referred to as a Si-bearing Ca-phosphate (1–7 wt.% SiO_2 and 35–45 wt.% P_2O_5) in Kaneda *et al.* (2001), was reported in plutonic angrites such as Angra dos Reis (Prinz *et al.*, 1977), LEW 86010 (Mckay *et al.*, 1988), Asuka 881371 (Prinz and Weisberg, 1995; Warren and Davis, 1995), D'Orbigny (Kaneda *et al.*, 2001; Mittlefehldt *et al.*, 2002) and NWA 1296 (Jambon *et al.*, 2005). In contrast to tsangpoite, matyhite received less attention in the past, probably because it has long been recognised to have a merrillite-like stoichiometry, and its structure determination by the synchrotron Laue method was inconclusive (e.g. Kaneda *et al.*, 2001; Mikouchi *et al.* 2001). In fact, as reported here, matyhite has a merrillite structure with high Ca, Fe, and low Na, Mg contents, in marked contrast to other known merrillite-group minerals from Martian meteorites or Lunar rocks (e.g. Britvin *et al.*, 2016; Hughes *et al.*, 2006, 2008; Jolliff *et al.*, 2006), and hence should be considered as a new merrillite-group mineral (Hwang *et al.*, 2016*b*).

Tsangpoite is named in honour of Professor Dr. Tsang-Po Yen (1914–1994), former senior geologist of the Geological Survey of Taiwan (1946–1974) and director of the Institute of Geophysics, National Central University, Taiwan (1974–1981). Prof. Yen contributed immensely to the mineralogical, petrological, ore-deposit and tectonic studies in Taiwan, including mineral characterisation for igneous and metamorphic rocks, structural and stress analyses for metamorphic rocks, identifying high-pressure rocks and metamorphic-belt subdivision, as well as metal and non-metal ore explorations. He published more than 90 papers during his academic career, and was highly respected by the Earth science community in Taiwan.

Matyhite is named in honour of Professor Dr. Ting-Ying H. Ma (1899–1979, middle name Hsüeh (H.) meaning snowy peak in Chinese), a distinguished palaeontologist who pioneered research into relations between coral growth rate, sea-water temperature, paleoclimate and paleogeography, with major contributions during 1930–1960 (cf. Yang and Oldroyd, 2003). He was one of the early advocates of continental drift. After World War II, Prof. Ma went to Taiwan, and was appointed the joint Director of the Department of Geology and the Institute of Oceanography of National Taiwan University and served from 1946 to 1950.

Type materials of tsangpoite and matyhite (as well as kuratite) are deposited in the collections of the Naturhistorisches Museum Wien, Vienna, Austria, inventory number Section D'Orbigny C-N1172-NH Wien, and the National Museum of Natural Science, Taiwan, ROC, inventory number NMNS007600-P020440.

Samples and analytical methods

Two polished slab samples with inventory number: Section D´Orbigny C-N1172-NH Wien (~1.5 cm × 1.5 cm) and M1173 (~2.0 cm × 3.0 cm in size) from the porous part and the dense part of D'Orbigny angrite, respectively, were loaned by the Naturhistorisches Museum Wien, Austria for the present study. Petrography of the D'Orbigny angrite has been described in detail by Mittlefehldt *et al.* (2002), Varela *et al.* (2003) and Kurat *et al.* (2004).

Thin sections of the slab samples were studied by optical microscopy (OM) and SEM under back-scattered electron (BSE) mode coupled with energy-dispersive X-ray (EDX) analyses using a JEOL JSM-7000F instrument operated at 15 kV. Transmission electron microscopic (TEM) imaging, single-crystal electron diffraction and TEM-EDX analyses were carried out using a JEOL 3010 analytical electron microscope (AEM) operated at 300 kV. More than three dozen TEM thin sections for imaging and electron diffraction studies were prepared using a SEIKO SMI-3050 focus ion beam microscope. Selected area electron diffraction (SAED) patterns were obtained from μm-sized tsangpoite and matyhite crystals at 120 cm camera length. For each diffraction pattern, only two or three of the shortest nonlinear reciprocal vectors were measured for *d*-spacing calculations. In general, the largest *d* spacing among a row of reflections with multiple *hkl* data was used for unit-cell refinement. The error of the *d*-spacing measurements of SAED patterns taken at a camera length of 120 cm and calibrated with an Al standard was estimated to be ±0.002 nm. Unit-cell parameters were refined using least-squares from measured *d* spacings extracted from electron-diffraction patterns.

Chemical analyses were undertaken using a JEOL JXA8500-F FE electron microprobe using wavelength dispersive spectroscopy (WDS) mode at 12 kV and 5 nA with a 2 μm beam diameter. Natural and synthetic mineral standards and diffracting crystals (in parentheses) used for calibration were: diopside for Si*K*α (TAP); rutile for Ti*K*α (PET); corundum for Al*K*α (TAP), chromium oxide for Cr*K*α (PET); hematite for Fe*K*α (LiF); tephroite for Mn*K*α (PET); periclase for Mg*K*α (TAP); Ni oxide for Ni*K*α (LiF); wollastonite for Ca*K*α (PET); albite for Na*K*α (TAP); adularia for K*K*α (PET); fluorapatite for P*K*α (PET); fluorite for F*K*α (TAP); tugtupite for Cl*K*α (PET); celestine for S*K*α (PET); Zn oxide for Zn*K*α (LiF); celestine for Sr*L*α (PET); Y-Al garnet (YAG) for Y*L*α (PET); LaP_5O_{14} for La*L*α (LiF); CeP_5O_{14} for CeLα (LiF); PrP_5O_{14} for Pr*L*β (LiF); NdP_5O_{14} for Nd*L*β (LiF); and YbP_5O_{14} for YbLα (LiF). Counting times for the peak of each element and backgrounds both above and below the peak were 20 s and 10 s, respectively. The detection limit for trace elements using the *K* or *L* line is ~600 ppm or 2000 ppm, respectively. Potential peak overlapping between elements was filtered by appropriate selection of the baseline counting position by pulse height analyser on X-ray counter. Targets for electron-probe analysis were selected carefully by secondary and back-scattered electron images.

The Raman spectrum of minute tsangpoite and matyhite grains ~5–10 μm in size were conducted by using a LABRAM HR micro-Raman spectrometer equipped with an Ar^+ laser with 514.5 nm excitation and a spatial resolution of 2–5 μm.

Results

General description of the D'Orbigny angrite and its phase assemblage

The texture of D'Orbigny can be described as a fluffy, but interlocking framework of anorthite (An) + olivine (Ol) (Fe-rich forsterite core and Ca-rich fayalite mantle) intergrowth plates of ~0.5–2 mm in thickness and up to ~5–10 mm in width/length.

They are overgrown by a kirschsteinite (Kir) layer and/or a Ca-rich fayalite (Fa)–Ca-deficient kirschsteinite intergrowth layer, with interstitial space filled by augite (Aug) with an Al–Ti-bearing hedenbergite (Hd) rim as well as a grain-boundary phase assemblage (cf. SEM montage in Supplementary material: Fig. S1*a*,*b*). The grain-boundary phase assemblage consists of: Fe sulfide (FeS, troilite); ulvöspinel; kuratite (Ku) (Hwang *et al.*, 2016*a*), described as Ti silicate or rhönite in the literature (Mittlefehldt *et al.*, 2002; Kurat *et al.*, 2004; Jambon and Boudouma, 2011); new mineral tsangpoite (Tsa) (Hwang *et al.*, 2015), described as Ca silico-phosphate or Si apatite in the literature (Kaneda *et al.*, 2001; Mittlefehldt *et al.*, 2002; Mikouchi *et al.*, 2001, 2010, 2011; Kurat *et al.*, 2004); new mineral matyhite (Ma) (Hwang *et al.*, 2016*b*), described as Ca phosphate in the literature (Mittlefehldt *et al.*, 2002; Kurat *et al.*, 2004); less commonly Na-bearing anorthite; and some unknown phases and voids (Fig. S1*a*,*b*). Besides the coarse Fa–Kir overgrowth over the forsterite core (Fig. S1*c*; hereinafter referred to as Fa–Kir overgrowth) commonly reported in the literature (e.g. Mittlefehldt *et al.*, 2002; Kurat *et al.*, 2004), there is another type of much finer symplectitic Fa–Kir intergrowth surrounding the resorbed Fe sulfide in the proximity of hedenbergite (Fig. S1*d*; hereinafter referred to as Fa–Kir symplectite). The representative compositions of the major phases in the D'Orbigny angrite are listed in Table S1 (Supplementary material – see below), and detailed petrographic descriptions and debate on the possible non-igneous origin of D'Orbigny can be found in Mittlefehldt *et al.* (2002), Kurat *et al.* (2004) and Varela *et al.* (2005).

Occurrences of tsangpoite and matyhite

Optical observations

Tsangpoite and matyhite occur specifically in well-defined but separated domains associated with Fe sulfide in the proximity of the contact between Fa–Kir overgrowth/symplectite and hedenbergite (see Fig. S1). Because of the high abundance, larger crystal sizes, and oriented rod-like growth morphology, tsangpoite was readily discernible petrographically by the relief and colour of the phases. Optical microscopy observations showed that groups of subparallel tsangpoite crystals with greyish colour usually nucleated at Fe sulfide and grew tangentially to the wall of Fa–Kir overgrowths into the space currently filled by brownish hedenbergite (Fig. 1*a*,*b*). Further OM observations showed that tsangpoite crystals with hexagonal cross-sections on the petrographic thin section surface could usually be traced back to the resorbed Fe sulfide using the focus (Fig. S2). Such elongated tsangpoite crystals frequently contain a central tube filled with opaque minerals of FeS + Mag ± ferrite (bcc Fe) ± Fe–S–O phases (Fig. 1*c*), as confirmed by electron imaging and diffraction (not shown). By contrast, because of the lower abundance and smaller sizes, it was more difficult to recognise/image matyhite in OM analyses. Nevertheless, some observations did show that greyish matyhite plate-shaped crystals usually nucleated and grew from the Fa–Kir symplectitic margin next to Fe sulfide into hedenbergite (Fig. 1*d*).

SEM-BSE observations

Observations from BSE analysis further showed that tsangpoite crystals either occur within Fe sulfide or Fa–Kir symplectite after Fe sulfide, or are currently embedded within the hedenbergite domain close to resorbed Fe sulfide. In the 'intact' Fe sulfide not in direct contact with hedenbergite, between either anorthite and the Fa–Kir overgrowth (Fig. 2*a*; Fa–Kir overgrowth not shown), or anorthite and ulvöspinel (Fig. 2*b*), or the impinged Fa–Kir overgrowths (Fig. 2*c*), tsangpoite crystals ~1–5 μm in diameter with hexagonal cross-section occur exclusively in the local partial-melting-like domain subjected to partial replacement of Fe sulfide by Mag + wüstite + Tsa ± celsian ± Al–Ti–Fe Spl (24–39 Usp, 24–31 Hc, 21–30 Mag; TEM-EDX; abbreviations according to Whitney and Evans, 2010) (Fig. 2*a*–*c*).

In contrast to rare tsangpoite at the aforementioned domains, abundant tsangpoite crystals occur at the resorbed Fe sulfide domains currently in contact with hedenbergite (Fig. 2*d*–*i*). At such domains, tsangpoite crystals reside within either residue Fe sulfide (Fig. 2*d*,*e*) or the Fa–Kir symplectite domain after Fe sulfide (Fig. 2*e*–*h*). The Fe sulfide crystal and the associated Fa–Kir symplectite appear to be relatively unstable and hence gradually dissociated/decomposed, thereby eventually exposing many tsangpoite crystals in a space of up to ~100–200 μm right in front of the resorbed Fe sulfide (Fig. 2*g*–*i*). Through-focus OM observations showed that many such tsangpoite crystals could be traced back to the decomposed Fe sulfide (e.g. Fig. 1*a*,*b*; Fig. S2). Tsangpoite crystals thus formed have an interesting size distribution. The large crystals (~10–20 μm) at the outermost apron away from the Fe sulfide core typically have irregular cross-sections (e.g. Fig. 2*f*–*i*) indicating rather high growth rates under high driving force. By contrast, the tsangpoite crystals close to or still within Fe sulfide or Fa–Kir symplectite are generally much smaller in size (~1–5 μm) and have a characteristic 'imperfect' hexagonal form by the $\{10\bar{1}0\}$ facets along with [0001]-oriented longitudinal grooves with rugged interiors, probably resulting from the matrix and/or solute hindrance on fast crystal growth (Figs 2*e*–*h*, 3*a*,*b*). In fact, tsangpoite tends to group as subparallel crystals aligned along the common [0001] growth direction to show similar cross-sections in the petrographic thin section (Fig. 3*b*,*c*). Besides the aforementioned tsangpoite with the 'normal' hexagonal crystal form, skeletal tsangpoite crystals, probably driven by the very high crystal growth rates, are also not uncommon (Fig. 3*d*). As noted in OM observations, the tsangpoite crystals that nucleated and grew from Fe sulfide frequently possess a central tube filled with opaque minerals (e.g. Fig. 1*c*). Such minerals, i.e. FeS + Mag ± ferrite ± Fe–S–O phases were also observed readily in SEM-BSE and EDX analyses of two subparallel tsangpoite crystals nucleated in an Fe sulfide, and grew outwards into the gap between two Fa–Kir overgrowths (Fig. 3e,f).

Unlike tsangpoite, matyhite was not found in the relatively 'intact' Fe sulfide at the sample domains away from hedenbergite (e.g. Fig. 2*a*–*c*). Instead, matyhite crystals frequently nucleated/grew within the Fa–Kir symplectite after Fe sulfide (Fig. 4*a*,*b*), yielding dendritic matyhite enclosed within Fa–Kir symplectite (Fig. 4*b*). Matyhite with high abundance of tiny Fe sulfide droplets and/or spherical voids also occurs frequently at the areas of contact between Fa–Kir symplectite and hedenbergite (Fig. 4*c*). Similarly to the case of tsangpoite, the gradual dissociation/decomposition of resorbed Fe sulfide and associated Fa–Kir symplectite also accounts for the exposure of some dendritic matyhite plates in the current hedenbergite phase, as illustrated nicely by the micrographs in Fig. 4*d*–*f*.

Tsangpoite and matyhite were also commonly distributed at the core and rim, respectively, in the same resorbed Fe sulfide crystals (Fig. 5*a*,*c*,*e*). For such occurrences, matyhite formed within Fa–Kir symplectite domains in contact with either hedenbergite or a Fa–Kir overgrowth (Fig. 5*a*,*c*). Groups of subparallel matyhite plates were frequently embedded within kuratite (e.g. Fig. 5*b*,*d*), albeit there are no specific crystallographic relationships in between

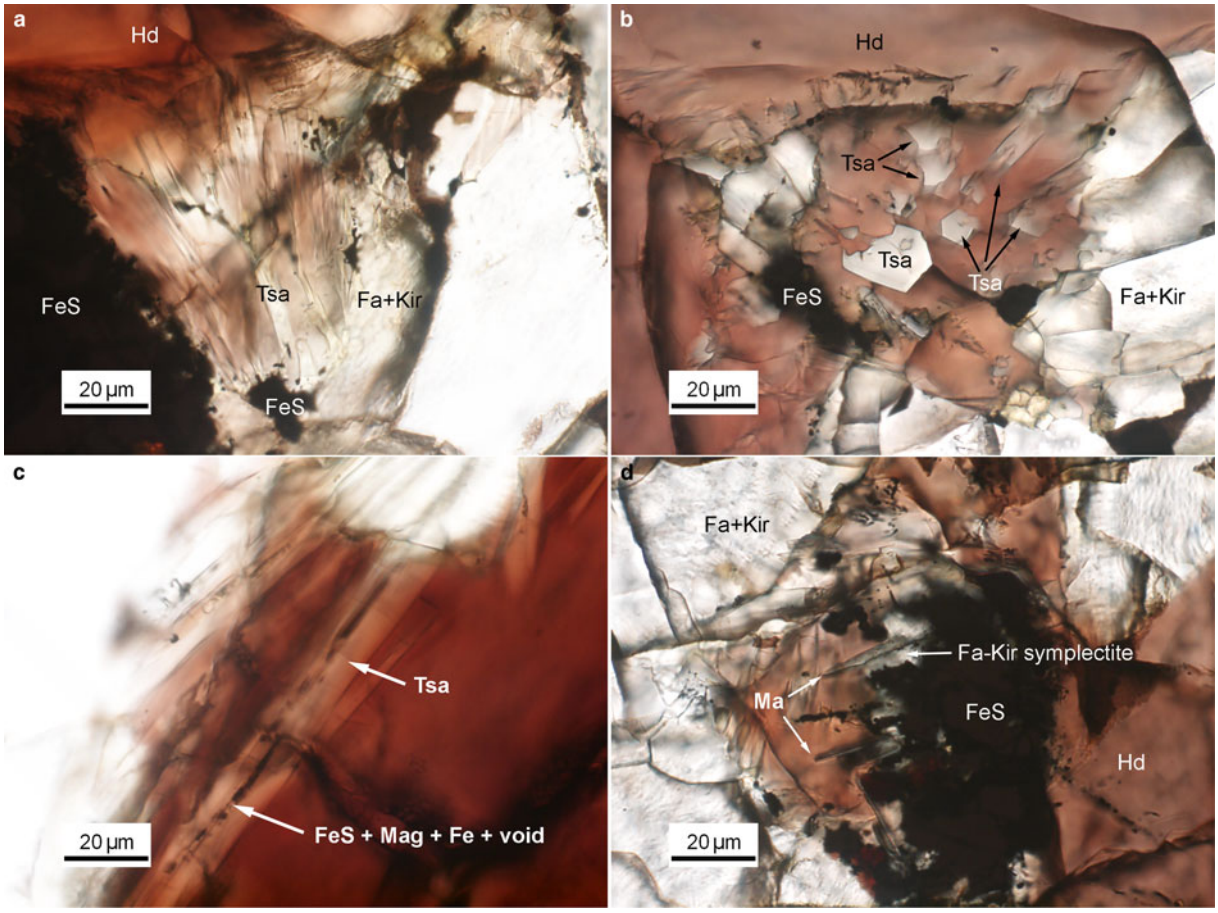

Fig. 1. Group of subparallel tsangpoite crystals that nucleated at FeS and grew tangentially to the wall of the Fa–Kir overgrowth: (*a*) viewed transversely; and (*b*) viewed nearly end-on. (*c*) The constant presence of segmental FeS + magnetite + Fe along the central tube of tsangpoite; and (*d*) group of dendritical matyhite plates that grew from the Fa–Kir symplectite margin of FeS. Image details: transmitted light, parallel Nicols.

based on electron diffraction (not shown). Although relatively rare, matyhite partly surrounding tsangpoite was noted, as shown in Fig. 5*e,f*. According to electron diffraction (not shown), there are no definite crystallographic relationships between such a tsangpoite–matyhite pair. Whereas the dendritic plates currently embedded within hedenbergite could grow to the size of ~30 μm (width) × ~5 μm (thick) (e.g. Fig. 4*f*), the matyhite dendritic plates within the Fa–Kir symplectite or kuratite are rather small, i.e. ~10 μm (width) × ~0.2 μm (thick) (e.g. Fig. 5*b,d*).

Crystallography

Tsangpoite

On the basis of least-squares refinement of 19 *d*-spacing measurements from electron diffraction patterns (Table 1), tsangpoite was determined conclusively to have a hexagonal unit cell with a = 9.489(4) Å, c = 6.991(6) Å, V = 545.1(6) Å^3 and Z = 2 for 12 oxygen atoms per formula unit, despite the absence of single-crystal XRD data because of crysal size restriction.

The systematic absence of reflections 000l with $l = 2n + 1$, as confirmed by tilting experiments away from the exact zone axis orientation to nullify double diffraction effects, indicates a 6_3 screw axis along c (Fig. 6*a,b*). The 'non-omission' of alternating columns of diffraction spots of {$hh2\bar{h}l$} or {$h\bar{h}0l$} with $l = 2n + 1$ in <11$\bar{2}$0> (Fig. 6*a*) and <1$\bar{1}$00> (Fig. 6*b*) zone axis patterns further excludes the possibility of the presence of c glide planes parallel to **c**. The intensity symmetry of the <0001> zone axis pattern, e.g. 2$\bar{3}$10 > 1$\bar{3}$20 (arrowed in Fig. 6*c*), further indicates that there are no 2-fold axes normal to the c axis. These considerations leave only $P6_3/m$ and $P6_3$ as possible space groups for tsangpoite. In this regard, it is noted that XRD data from a relatively large calcium silico-phosphate crystal (tsangpoite) from the NWA angrite 4590 indicated a hexagonal $P6_3/m$ structure with a = 9.479 and c = 6.97 Å (Mikouchi *et al.*, 2011), in close agreement with the electron diffraction results presented here. Note that due to space-group specification, the <*hkil*> family may show different intensity symmetry, cf. Fig. S3*a,b* for the case of <$\bar{5}$140> and Fig. S3*g,h* for the case of <$\bar{5}$149$\bar{}$>. The ten relatively strong reflections in order of decreasing d spacing (in Å) are: $\bar{1}\,\bar{1}$21 (3.94), 0002 (3.50), 2$\bar{3}$10 (3.10), 2$\bar{3}$11 and 1$\bar{3}$21 (2.83), 1$\bar{2}\bar{1}\bar{2}$ (2.82), 3$\bar{3}$00 (2.74), 20$\bar{2}\bar{2}$ (2.66), $\bar{1}$4$\bar{3}$0 (2.28), $\bar{2}\,\bar{2}$42 (1.97) and $\bar{4}$402 (1.77) (Fig. S3). The d spacings, symmetry, lattice parameters, and unit-cell correspondence of tsangpoite, hydroxylapatite, as well as the high-temperature hexagonal solid-solution phase and the low-temperature intermediate phases in the system Ca_2SiO_4–$Ca_3(PO_4)_2$ are compiled in Tables 1 and 2 for comparison (see Discussion).

Matyhite

Based on the least-squares refinement of 20 *d*-spacing measurements from electron diffraction patterns (Table 3), matyhite

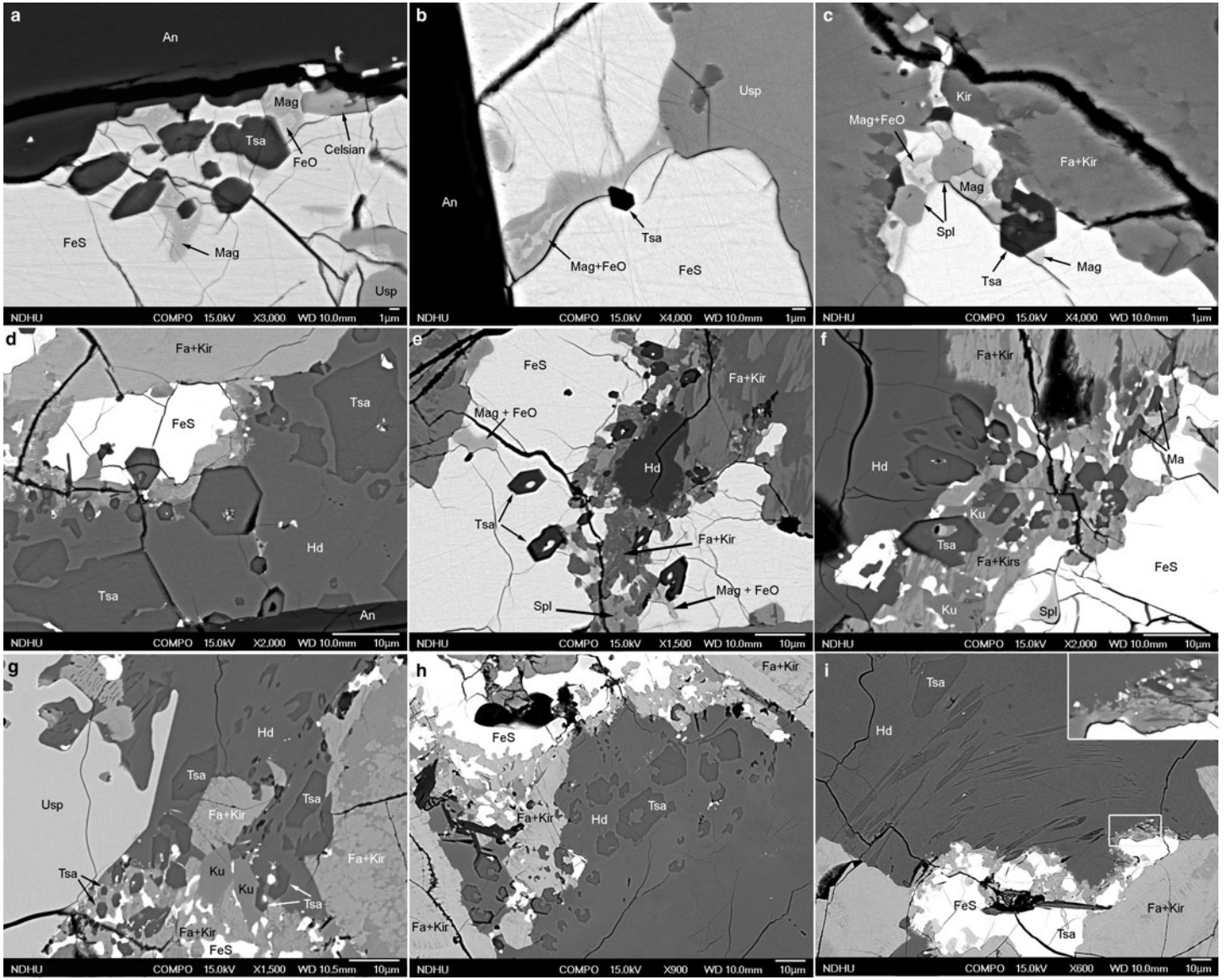

Fig. 2. Back-scatter electron micrographs showing the oxidation assemblage: FeS => Tsa + Mag + FeO ± celsian ± Al–Ti–Fe Spl within the 'intact' FeS at (*a*) contact of anorthite and Fa + Kir overgrowths (Fa + Kir overgrowths not shown), (*b*) contact of anorthite and ulvöspinel or (*c*) the impinged Fa–Kir overgrowths, and abundant tsangpoite crystals within (*d*,*e*) residue FeS, or (*d–h*) the Fa + Kir symplectite after FeS in the proximity of hedenbergite, as well as (*g–i*) the dissociation/decomposition of the Fa–Kir symplectite and the formation of well-defined tsangpoite domains in front of resorbed FeS. Note the partial melting-like Mag + FeO domain in (*a–c*), the bimodal size distribution of tsangpoite in (*d–i*), the tsangpoite + kuratite association in (*g*), as well as the dissociation-like feature of resorbed FeS in (*h*,*i*). Abbreviations according to Whitney and Evans (2010); Tsa – tsangpoite.

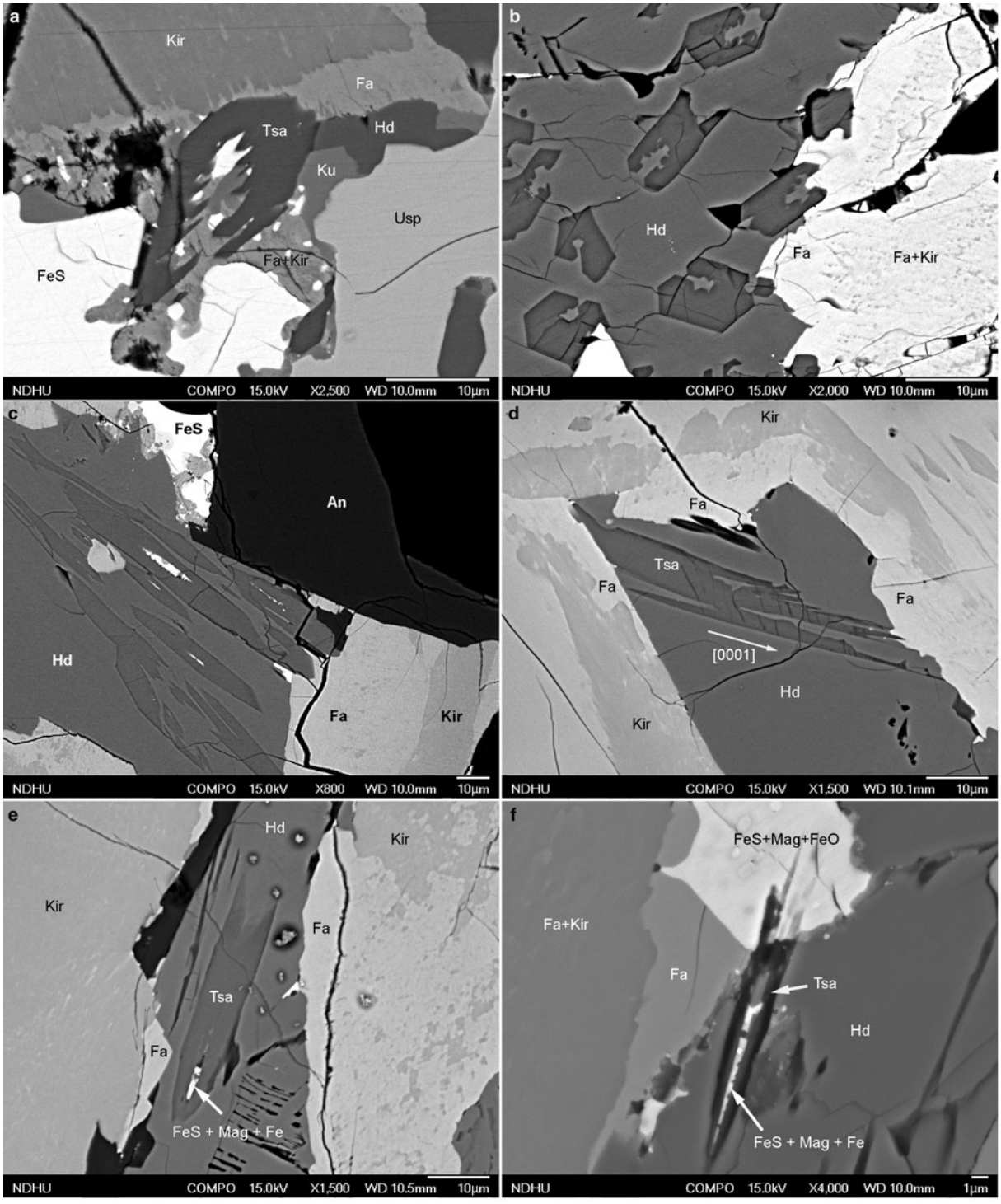

Fig. 3. Back-scatter electron micrographs showing: (*a*,*b*) imperfect hexagonal cross-section with longitudinal groove of tsangpoite in Fa–Kir symplectite; (*b*,*c*) groups of subparallel tsangpoite crystals with similar cross-section morphologies exposed in hedenbergite; (*d*) a highly defective skeletal tsangpoite crystal viewed transversally; and (*e*,*f*) two subparallel oblique tsangpoite crystals originated from the same FeS crystal with central tube filled by FeS + Mag + Fe.

was determined conclusively to have a trigonal unit cell with $a = 10.456(7)$ Å, $c = 37.408(34)$ Å, $V = 3541.6(4.8)$ Å^3 and $Z = 6$ for 28 oxygen atoms per formula unit. The set of d spacings and the refined unit-cell parameters of matyhite in the present study are comparable to those of other merrillite-group minerals, whitlockite and synthetic β-TCP (Tables 3 and 4). The systematic absence of reflections $000l$ with $l \neq 6n$ (Fig. 6*d*), absence of reflections with $-h + k + l \neq 3n$ (Fig. 6*d*), as well as the absence of reflections hhl with $l \neq 3n$ (Fig. 6*e*) indicate that matyhite has $R3c$ space group, which is the common space group for whitlockite/merrillite-group minerals. The nine relatively strong reflections in order of decreasing d spacing (in Å) are: $0\bar{1}14$ (6.52), $2\bar{1}\bar{1}0$ (5.24), $0\bar{1}1.10$(3.46), $3\bar{1}\bar{2}4$ (3.21), $30\bar{3}0$ (3.02), $0\bar{2}2.\bar{1}0$ (2.88), $\bar{3}128$ (2.75), $4\bar{2}\bar{2}0$ (2.62) and $3\bar{1}\bar{2}.10$ (2.53) (Fig. S4).

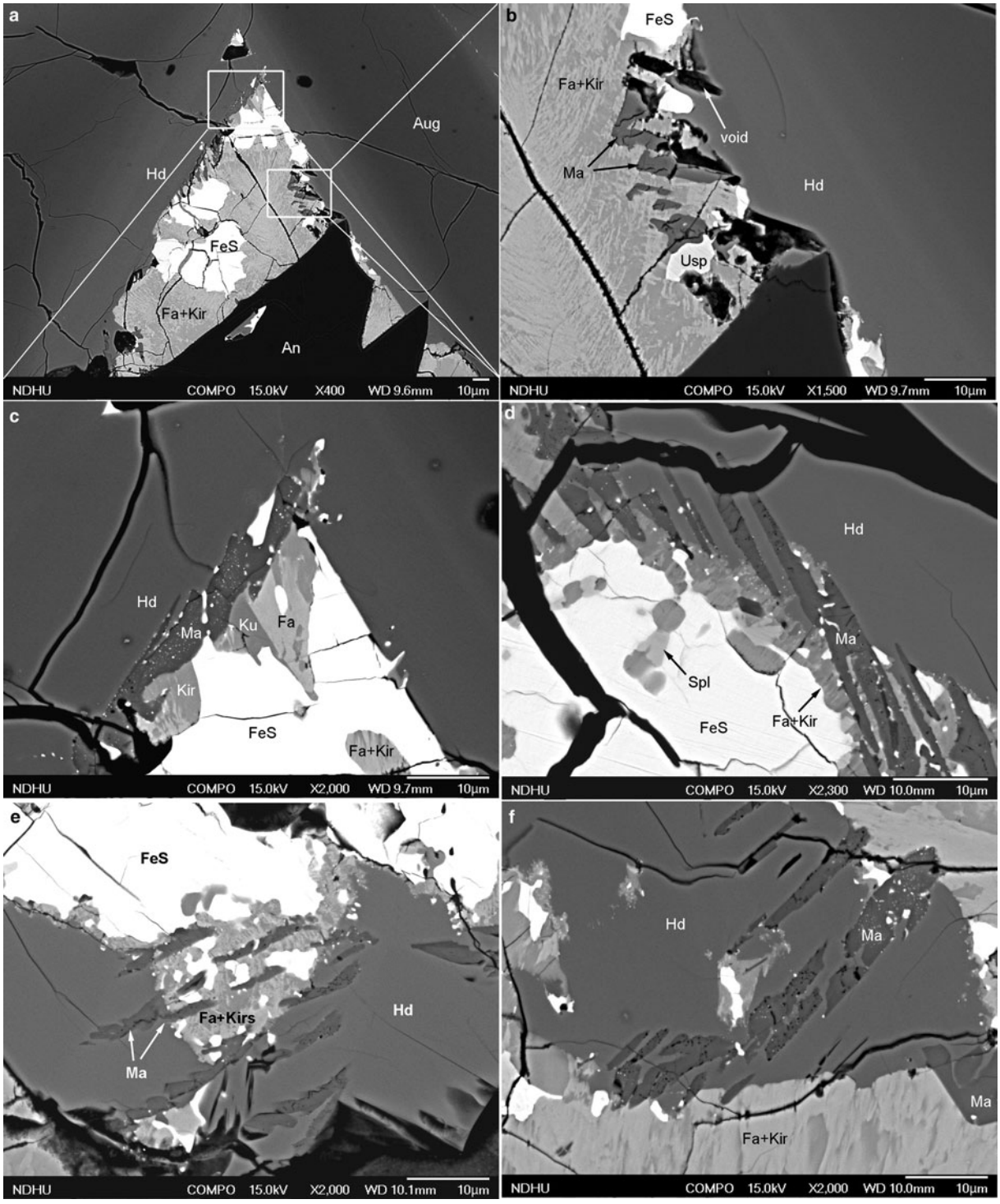

Fig. 4. Back-scatter electron micrographs showing the formation of matyhite plates (*a*,*b*) within Fa–Kir symplectite; (*c*) tangential to the contact between Fa–Kir symplectite and hedenbergite; and (*d*–*f*) the dissolution/decomposition of Fa–Kir symplectite and the consequential exposure of dendritical matyhite plates in hedenbergite. Note the frequent inclusion of abundant FeS droplets and/or spherical voids in matyhite (*c*–*f*).

TEM imaging

Transmission electron microscopy bright field (TEM BF) images of tsangpoite within hedenbergite or Fa–Kir symplectite compiled in Fig. 7 show the characteristic imperfect [0001] cross-sections of tsangpoite (Fig. 7*a*), the frequent association of tsangpoite and fayalite (Fig. 7*a*,*b*), Fe sulfide + Mag at the central tube of tsangpoite (Fig. 7*c*), as well as the interesting, grain-coalescence-like zigzag outline of the interior of an open, [0001]-oriented groove of tsangpoite similar to that shown in Fig. 3*a*,*b* (Fig. 7*d*). Several occasional crystallographic orientation relationships were found between tsangpoite and the olivine matrix, e.g. $<0001>_{Tsa}$ ~//~ $<100>_{Ol}$ and $\{1\bar{1}00\}_{Tsa}$ ~//~

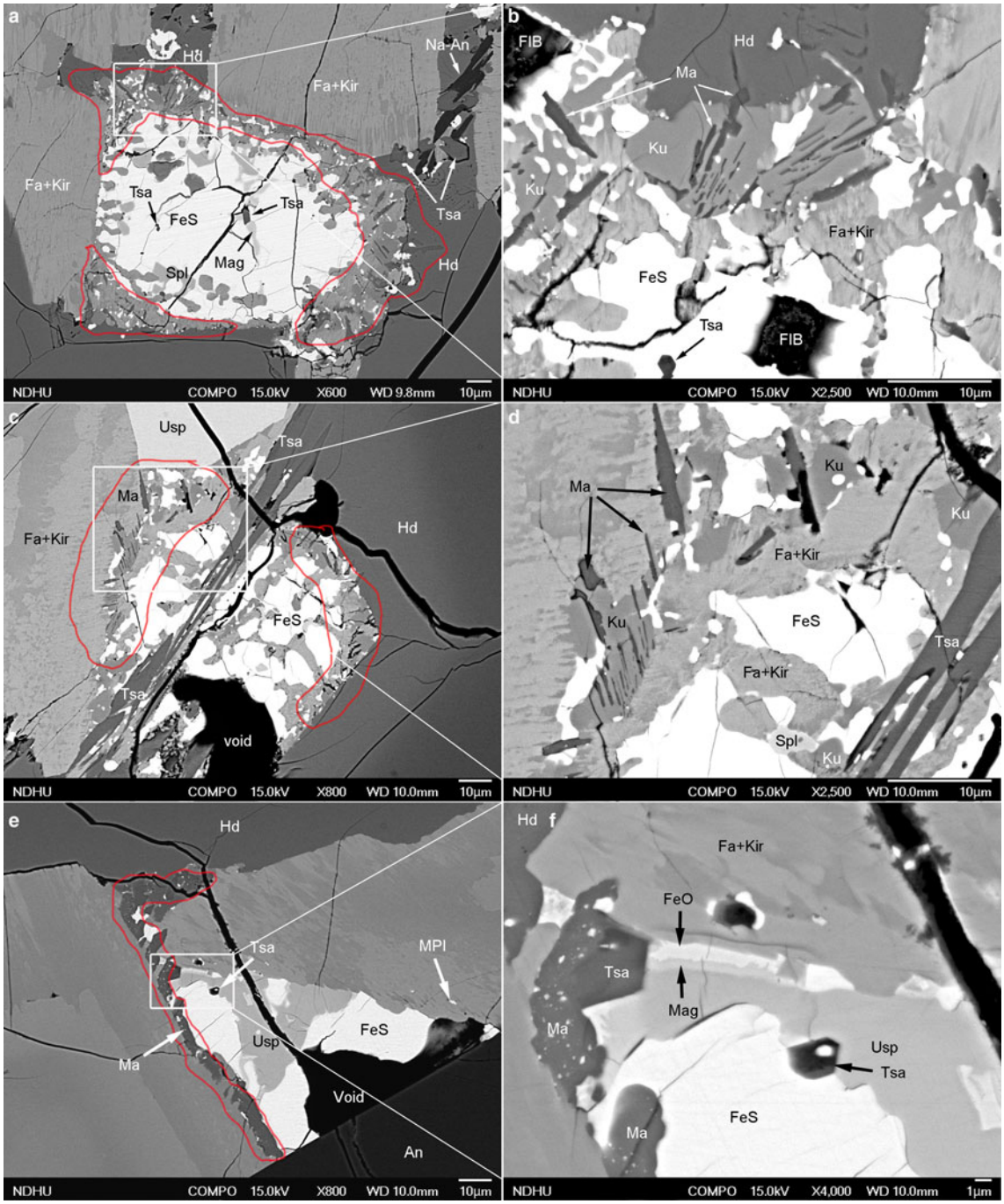

Fig. 5. Back-scatter electron micrographs showing the concurrent presence of (*a–d*) tsangpoite at the core and matyhite (outlined in red) at the rim of resorbed Fe sulfide; and (*e*,*f*) tsangpoite at the core and matyhite (outlined in red) at the areas of contact with Fa–Kir overgrowth of a partially altered Fe sulfide. The skeletal morphology of tsangpoite crystal was noted in (c,d) and the occasional contact between tsangpoite and post-dated matyhite was noted in (*f*).

$\{011\}_{Ol}$ for the pair in Fig. 7*a* (tsangpoite appears to be detached from the olivine–hedenbergite boundary, leaving a negative crystal shape of olivine), or $<11\bar{2}6>_{Tsa}$ ~//~ $<210>_{Ol}$ and $\{1\bar{1}00\}_{Tsa}$ ~//~ $\{001\}_{Ol}$ for the pair in Fig. 7*c*, or $<11\bar{2}0>_{Tsa}$ ~//~ $<014>_{Ol}$ and $\{1\bar{1}00\}_{Tsa}$ ~//~ $\{34\bar{1}\}_{Ol}$ (not shown), or $<11\bar{2}3>_{Tsa}$ ~//~ $<110>_{Ol}$ and $\{1\bar{1}00\}_{Tsa}$ ~//~ $\{001\}_{Ol}$ (not shown), or $<11\bar{2}3>_{Tsa}$ ~//~ $<112>_{Ol}$ and $\{1\bar{1}00\}_{Tsa}$ ~//~ $\{1\bar{1}0\}_{Ol}$ (not shown).

Although quite rare, as noted from SEM analyses, a tsangpoite + matyhite association was observed occasionally (see Fig. 5*f*). TEM BF images show the phase distribution/arrangement of tsangpoite with hexagonal cross-section, matyhite with tabular cross-section and Fe sulfide, as well as the surrounding hedenbergite matrix in one TEM thin section prepared selectively from the tsangpoite + matyhite association in Fig. 5*f* (Fig. 7*e*). Electron diffraction showed that the three tsangpoite crystals in this thin section are nearly parallel to each other along their *c* axis (<3–5° off), consistent with the SEM observations. A subgrain boundary is not common, but was found occasionally within one tsangpoite crystal (Fig. 7*e*). Despite the fact that tsangpoite appears to be oriented within the hedenbergite matrix, as also observed in

Table 1. Observed and calculated *d* spacings (Å) for tsangpoite and related phases.

d_{obs}	d_{calc}	$Ca_{11.1}(PO_4)_{1.8}(SiO_4)_{4.2}$ Fukuda *et al.* (1997)[1]	$Ca_7(PO_4)_2(SiO_4)_2$ Bredig (1942)	$Ca_5(PO_4)_2(SiO_4)$ Nurse *et al.* (1959)[2]	Hydroxylapatite JCPDS file 09-0432[3]	*h*	*k*	*l*
8.22	8.217				8.17(12)	1	0	0
5.32	5.325				5.26(6)	1	0	1
4.74	4.744				4.72(4)	1	1	0
3.94	3.926	3.91(30)	3.93 (w)	3.98(40)	3.88(10)	1	1	1
3.54	3.542				3.51(2)	2	0	1
3.50	3.496	3.56(<10)	3.52 (w)	3.50(<10)	3.44(40)	0	0	2
3.21	3.217				3.17(12)	1	0	2
3.10	3.106			3.10(<10)**	3.08(18)	1	2	0
2.83	2.838	2.83(30)	2.86 (st)	2.94(60)	2.81(99)	1	2	1
2.82	2.814				2.78(60)	1	1	2
2.74	2.739	2.70(99)	2.70 (st)	2.70(40)	2.72(60)	3	0	0
2.66	2.662				2.63(25)	2	0	2
2.55	2.550				2.53(6)	3	0	1
2.37		2.33(<10)	2.33 (vw)			2	2	0*
2.28	2.279	2.22(10)	2.22 (vw)		2.26(20)	1	3	0
1.97		1.96(20)	1.96 (st)	1.99(30)	1.94(30)	2	2	2*
1.97	1.971					4	0	1
1.91	1.909		1.86 (vw)**		1.89(16)	1	3	2
1.80	1.793				1.78(12)	4	1	0
1.77	1.771	1.78(<10)	1.76 (m)		1.75(16)	4	0	2
1.64	1.640	1.66(<10)	1.67 (w)			1	1	4

[1]Quenched from 1500°C; [2]high-temperature camera powder measurements at ~1500°C; [3]powder diffraction files from the International Centre for Diffraction Data (http://www.icdd.com/).
*Duplicated data, not used for lattice parameters refinement; **reflection not consistent with α-Ca_2SiO_4 unit cell.
The strongest reflections are marked in bold; w – weak; st – strong; vw – very weak; m – moderate.

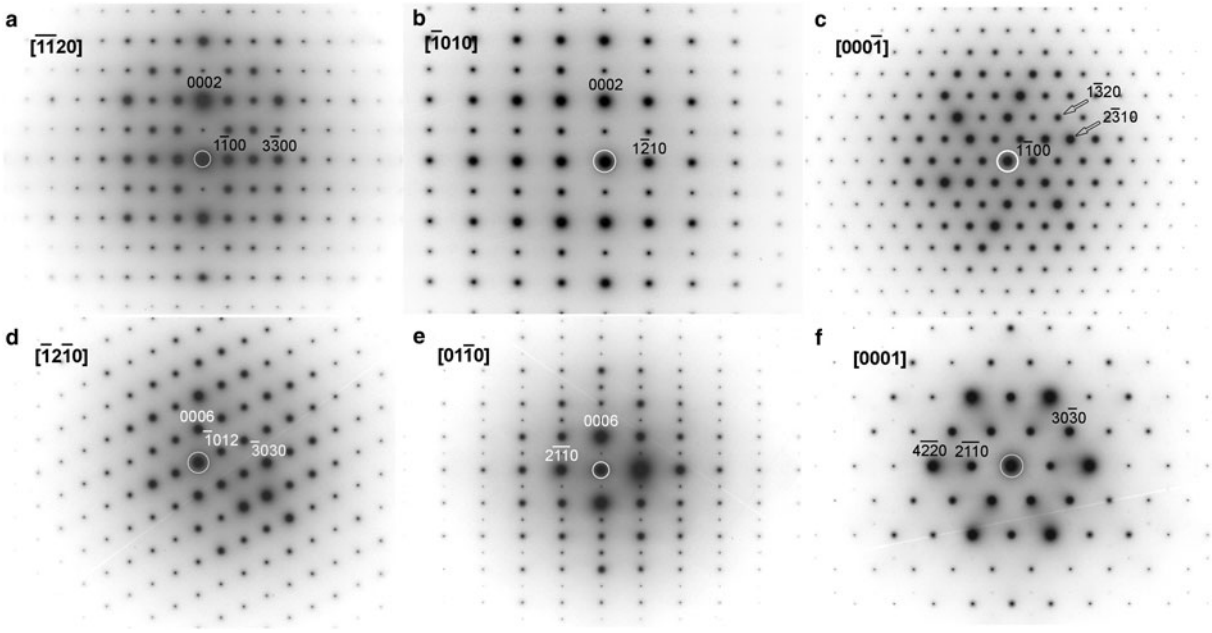

Fig. 6. The representative electron-diffraction patterns of (*a–c*) tsangpoite, and (*d–f*) matyhite in the principal zone axes.

SEM micrographs, there are no specific crystallographic orientation relationships between them, according to an electron diffraction study (not shown). At the contact between tsangpoite and matyhite, a thin layer depleted in Si (compared to tsangpoite) was noted by TEM-EDX analysis (insert in Fig. 7*e*). Figure 7*f* is a TEM BF image of another focused ion beam thin section prepared selectively from the tsangpoite–kuratite association in Fig. 2*g* showing the association of tsangpoite + kuratite in Fa–Kir symplectite (see Fig. 2*g*). Note that the tiny tsangpoite crystal branching into two halves and facetted by {1$\bar{1}$00} and {1$\bar{1}$02} planes probably nucleated at the central Fe sulfide and grew along the crystallographic *c* axis. There is no definite crystallographic orientation relationship between tsangpoite and kuratite, according to electron diffraction.

The results from TEM BF imaging and electron diffraction showed that the matyhite plates within a dendritic bundle in hedenbergite usually have approximately similar crystallographic orientation and habit in space (up to several degrees off). The

Table 2. Lattice parameters of tsangpoite, α-Ca_2SiO_4, silico-phosphate and hydroxylapatite.

Mineral	Composition	Notes	Space group	Cell parameters (Å)		
				a	*b*	*c*
Tsangpoite						
Tsangpoite (D'Orbigny)	$(Ca_{8.07}\square_{0.84}Fe^{3+}_{0.75}Ti_{0.20}Al_{0.06}REE_{0.02}Sr_{0.02}Y_{0.01}Cr_{0.01}Ni_{0.01}Zn_{0.01})_{\Sigma 10.0}$ $[(P_{3.99}Si_{1.97}S_{0.06})_{\Sigma 6.02}(O_{23.72}F_{0.23}Cl_{0.04})_{\Sigma 23.99}]$		$P6_3$ or $P6_3/m$	9.49	9.49	6.99
Tsangpoite (NWA 4590)	$(Ca_{8.78}\square_{0.71}Fe^{3+}_{0.34}Ti_{0.08}Al_{0.08}Mn_{0.01})_{10.0}[(P_{4.64}Si_{1.41})_{\Sigma 6.05}O_{24}]$	[1]		9.48	9.48	6.97
High-*T* phases in Ca_2SiO_4–$Ca_3(PO_4)_2$ system						
	α-Ca_2SiO_4	[2],[3]	$P\bar{3}m1$ *or* $6_3/mmc$	5.53	5.53	7.31
	$Ca_{11.1}(PO_4)_{0.9}(SiO_4)_{4.2}$	[4]		5.40	5.40	7.13
	$Ca_{15}(PO_4)_2(SiO_4)_6$	[5]	$P6_3/mmc$	5.39	5.39	7.13
	$Ca_7(PO_4)_2(SiO_4)_2$	[6]		5.38	5.38	7.10
	$Ca_5(PO_4)_2(SiO_4)$	[7]		5.51	5.51	7.10
	$(Ca_{1.97}Na_{0.16})(Si_{0.92}Al_{0.05}Fe_{0.04})O_4$	[8]		5.43	5.43	7.05
	$(Ca_2SiO_4{\cdot}0.135Na_2O{\cdot}0.068Fe_2O_3)$	[9]		5.40	5.40	7.00
Low-*T* phases in Ca_2SiO_4–$Ca_3(PO_4)_2$ system						
Flamite	$Ca_{15}(PO_4)_2(SiO_4)_6$	[10], [11]	$Pnm2_1$	9.40	21.71	6.83
Nagelschmidtite	$Ca_7(PO_4)_2(SiO_4)_2$	[12]	$P6_1$	10.78	10.78	21.42
Silicocarnotite	$Ca_5(PO_4)_2(SiO_4)$	[13]	*Pnma*	6.72	15.45	10.09
Hydroxylapatite	$Ca_{10}(PO_4)6OH_2$	[14]	$P6_3/m$	9.42	9.42	6.88

[1] Mikouchi *et al.* (2011); [2] Yamaguchi *et al.* (1963), 1500°C; [3] Mumme *et al.* (1996); [4] Fukuda *et al.* (1997), impurity stabilised α-Ca_2SiO_4, quenched from 1500°C; [5] Widmer *et al.* (2015), quenched from 1300°C, with diffuse flamite-like reflections; [6] Bredig (1942; 1943); [7] Nurse *et al.* (1959), refined from 5 *d* spacings at ~1500°C; [8] Fukuda *et al.* (1993), impurity stabilised α-Ca_2SiO_4, quenched from 1400°C; [9] Bredig (1943), impurity stabilised α-Ca_2SiO_4; [10] Saalfed and Klaska (1981); [11] Gfeller *et al.* (2015); [12] Widmer *et al.* (2015); [13] Galuskin *et al.* (2016); and [14] Marchat *et al.* (2013).

Table 3. Observed and calculated *d* spacings (Å) for matyhite* and related phases.

d_{obs}	d_{calc}	Merrillite [1]	Ca-merrillite [2]	Ferromerrillite [3]	*REE*-merrillite [4]	Whitlockite [5]	β-Tcp [6]	*h*	*k*	*l*
8.14	8.150	8.06(7)	8.08(11)	8.09(18)	8.02(23)	8.06(7)	8.14(15)	0	1	2
6.52	6.505	6.44(19)	6.45(21)	6.46(33)	6.41(34)	6.44(30)	6.50(21)	1	0	4
6.23	6.235	6.17(4)	6.18(4)	6.18(9)	6.15(6)	6.18(12)	6.23(4)	0	0	6
5.24	5.228	5.17(25)	5.18(24)	5.20(20)	5.15(37)	5.17(43)	5.22(25)	1	1	0
4.82	4.821	-	-	4.79(2)	4.75(1)	4.77(1)	4.81(2)	1	1	3
4.40	4.400	4.35(9)	4.36(7)	4.37(9)	4.33(3)	-	4.39(7)	2	0	2
4.16	4.155	4.11(1)	-	4.12(3)	4.09(2)	4.12(2)	4.15(2)	0	1	8
4.01	4.006	-	-	3.97(3)	3.95(2)	-	4.00(2)	1	1	6
3.46	3.457	3.42(25)	3.43(25)	3.42(20)	3.41(29)	3.43(36)	3.46(26)	1	0	10
3.35	3.367	3.33(10)	3.34(8)	3.34(11)	3.31(7)	3.33(7)	3.36(8)	1	2	2
3.26	3.254	3.22(4)	3.23(4)	3.23(4)	3.21(2)	3.22(3)	3.25(6)	1	1	9
3.21	3.214	3.18(48)	3.19(51)	3.19(81)	3.16(52)	3.18(64)	3.21(56)	2	1	4
3.02	3.018	2.99(14)	2.99(14)	2.99(14)	2.97(15)	2.98(11)	3.01(13)	3	0	0
2.88	2.884	2.85(99)	2.86(99)	2.86(99)	2.84(99)	2.86(99)	2.88(99)	0	2	10
2.75	2.762	2.73(19)	2.74(20)	2.74(21)	2.72(20)	2.73(31)	2.76(20)	1	2	8
2.68	2.678	2.65(5)	2.66(6)	2.66(7)	2.64(4)	2.65(7)	2.68(6)	1	1	12
2.62	2.614	2.59(63)	2.59(64)	2.59(73)	2.57(70)	2.58(85)	2.61(70)	2	2	0
2.53	2.525	2.50(14)	2.50(13)	2.50(13)	2.49(13)	2.50(9)	2.52(11)	2	1	10
2.25	2.264	2.24(8)	2.24(8)	2.24(10)	2.23(7)	2.25(7)	2.26(10)	1	0	16
1.83	1.832	1.81(5)	1.82(4)	1.82(8)	1.81(5)	1.82(4)	1.83(4)	0	1	20
1.71	1.712	1.69(7)	1.70(7)	1.70(11)	1.69(7)	1.70(7)	1.71(8)	3	0	18

*The strongest reflections are marked in bold.
[1] Suizho meteorite (Xie *et al.*, 2015), *American Mineralogist* Crystal Structure Database (amcsd)-0020386; [2] Angra dos Reis (Dowty, 1977), amcsd-0018313; [3] Shergotty meteorite (Britvin *et al.*, 2016). [4] Lunar rock, Fra Mauro Formation (Hughes *et al.*, 2006), amcsd-0004238; [5] Palermo Quarry (Gopal and Calvo, 1972), amcsd-0000445; and [6] Dickens *et al.* (1974), JCPDS file 70-2065 (powder diffraction files from the International Centre for Diffraction Data, http://www.icdd.com/).

majority of thick matyhite plates within the hedenbergite analysed are ~(0001) plates with segments of flat (0001) facets (Fig. 8*a*), although minor ~{11$\bar{2}$0} plates were also observed (Fig. 8*b*). The presence of abundant voids of various morphologies in some matyhite plates within hedenbergite can be seen clearly in Fig. 8*b*,*d* (arrowed). As for the thin matyhite plates within kuratite, TEM imaging showed that a dendritic bundle of thin matyhite plates could be embedded by multiple kuratite crystals (Fig. 8*c*) or by a single kuratite crystal (Fig. 8*d*). The matyhite plates could be flat (e.g. Fig. 8*c*) or wavy (e.g. Fig. 8*d*), and the mis-orientations in-between (up to ~30°) are generally larger than that in hedenbergite. Minor hedenbergite in good crystallographic orientation relationships to kuratite, as well as Fe sulfide in random orientations, were also frequently noted in such domains (e.g. Fig. 8*c*). The matyhite crystals in kuratite could be either ~{11$\bar{2}$6} plates (Fig. 8*c*,*d*), or ~{10$\bar{1}$4} plates (Fig. 8*e*,*f*). The bundle of thin ~{10$\bar{1}$4} plates within fine Fa–Kir symplectite also contain many sub-grain boundaries (Fig. 8*f*), in addition to the irregular voids (Fig. 8*f*).

Raman spectroscopy

The Raman spectrum of tsangpoite shows six bands: 437–448 and 460–465 (ν_2 PO_4), 591–601 (ν_4 PO_4), 867–871 (Si–O stretching),

Table 4. Lattice parameters of merrillite-group minerals, whitlockite, and synthetic β-tricalcium phosphate.

Mineral	Ref.	Composition	Trigonal *a*, *c* (Å)
Matyhite		$(Ca_{8.91}Sr_{0.05}REE_{0.04})_{\Sigma 9.0}(\square_{0.52}Ca_{0.42}Na_{0.05}K_{0.01})_{\Sigma 1.0}(Fe^{2+}_{0.68}Fe^{3+}_{0.26}Al_{0.02}Ti_{0.01}Mn_{0.01}Zn_{0.01})_{\Sigma 0.99}(P_{6.75}Si_{0.26})_{\Sigma 7.01}O_{28.02}$ ~ $Ca_9(Ca_{0.5}\square_{0.5})Fe(PO_4)_7$	10.46, 37.41
Merrillite	[1]	$Ca_9Na_1(Mg_{0.95}Fe_{0.06})(PO_4)_7$	10.34, 37.02
Ca-Merrillite	[2]	$Ca_9(Ca_{0.55}\square_{0.45})(Mg_{0.78}Fe_{0.22})(PO_4)_7$ ~ $Ca_9(Ca_{0.5}\square_{0.5})Mg(PO_4)_7$	10.36, 37.11
Ferromerrillite	[3]	$Ca_{9.00}(Na_{0.6}Ca_{0.07})_{\Sigma 0.67}(Fe_{0.53}Mg_{0.4})_{\Sigma 0.93}P_{7.08}O_{28}$ ~ $Ca_9NaFe(PO_4)_7$	10.37, 37.22
REE-Merrillite	[4]	$[(REE,Y)_{0.69}Ca_{8.41}]_{\Sigma 9.10}(Na_{0.195})(Mg_{0.72}Fe_{0.31}Mn_{0.01})_{\Sigma 1.04}(PO_4)_7$ ~ $(REE,Y)Ca_8Mg(PO_4)_7$	10.29, 36.88
Whitlockite	[5]	$Ca_{9.1}Mg_{0.59}Fe_{0.42}H_{0.81}(PO_4)_7$ ~ $Ca_9MgH(PO_4)_7$	10.33, 37.10
β-tricalcium phosphate	[6]	$Ca_9(Ca_{0.5}\square_{0.5})Ca(PO_4)_7$	10.44, 37.8

[1] Suizho meteorite (Xie *et al.*, 2015); [2] Angra dos Reis (Dowty, 1977); [3] Shergotty meteorite (Britvin *et al.*, 2016); [4] Lunar rock, Fra Mauro Formation (Hughes *et al.*, 2006); [5] Palermo Quarry (Gopal and Calvo, 1972); [6] Dickens *et al.* (1974).

959–961 (ν_1 PO_4, strongest) and ~1019 (ν_3 PO_4), as well as a weak and broad band at ~630–700 cm^{-1} (Fig. 9*a*; see also Mikouchi *et al.*, 2010). This spectrum basically resembles that of nagelschmidtite (402–439, 587, 642–647, 857, 961–963, 1058 and 1084 cm^{-1}; Lugo *et al.*, 2015; Rabadan-Ros *et al.*, 2016), silicocarnotite (418, 593, ~634 or ~700 (in 2 analyses), 854, 959–963 and 1000–1150 cm^{-1}; Serena *et al.*, 2014; 2015; 397, 474, 557, 584, ~626–734 with a series of vibrations, 850, 957 and ~1000–1100 cm^{-1}; Galuskin *et al.*, 2016), and probably Si-substituted hydroxylapatite with the ~630–700 cm^{-1} band missing (~450, ~600, 847, 954–972 and ~1050 cm^{-1}; Gomes *et al.*, 2011). The low intensity band at ~630–700 cm^{-1} of tsangpoite probably has a similar cause as the un-assigned ~645 cm^{-1} band of nagelschmidtite in Lugo *et al.* (2015) and Rabadan-Ros *et al.* (2016), the ~700 cm^{-1} band of silicocarnotite in Serena *et al.* (2014) considered to be related to Si–O–Si bending modes (e.g. Ibáñez *et al.*, 2007), or the ~626–734 cm^{-1} band of silicocarnotite which has a series of vibrations with the 'strongest' at 640 cm^{-1} attributed to ν_4 PO_4 by Galuskin *et al.* (2016). The lack of a Raman peak at ~2000, ~3000 or ~3500 cm^{-1}, characteristic of OH vibrations, indicates that tsangpoite is OH free. Investigations using micro Fourier-transform infrared of a relatively large calcium silico-phosphate crystal (tsangpoite) from the NWA angrite 4590 also showed no OH content (Mikouchi *et al.*, 2011). The broader and weaker SiO_4 vibrations at ~850 cm^{-1}, and probably also 630–700 cm^{-1}, of tsangpoite compared to that of nagelschmidtite and silicocarnotite could be due to structural vacancies and aliovalent cations accompanying the substitution of Si for P for volume and charge compensation to shift vibration frequencies.

The Raman spectrum of matyhite shows several scattering bands near 414 (ν_2 PO_4), 458 (ν_2 PO_4), 573 (ν_4 PO_4), 629 (ν_4 PO_4), 953 (ν_1 PO_4), 959 (ν_1 PO_4) and 1097 (ν_3 PO_4) cm^{-1} (Fig. 9*b*), resembling that of synthetic merrillite or β-tricalcium phosphate (de Aza *et al.*, 1997, Mikouchi *et al.*, 2001; Jolliff *et al.*, 2006; Jillavenkatesa and Condrate Sr., 1998). The lack of a Raman peak at ~3500 cm^{-1} (not shown), characteristic of OH vibration, demonstrates that matyhite is OH free. The 662, 772, 840 and 1008 cm^{-1} bands (arrowed) in Fig. 9*b* are due to the hedenbergite matrix.

Composition

Tsangpoite

Eight analyses from four tsangpoite crystals and their averages are given in Table 5. Having similar reflection data to the α-Ca_2SiO_4-derived structure or apatite structure (see Discussion), tsangpoite lattice sites can be assigned by the formula $M_{10}T_6O_{24}$ of silico-phosphate in the binary Ca_2SiO_4–$Ca_3(PO_4)_2$ system, or the formula $M_{10}T_6O_{24}X_2$ of the apatite structure where the tetrahedral *T*-site atoms are P + Si + S = 6 (0.05) and other cations are at octahedral *M* sites. The empirical formula based on 6 P + Si + S and 24 O + F + Cl or 24 O, with rounding errors, is then $(Ca_{8.07}\square_{0.84}Fe^{3+}_{0.75}Ti_{0.20}Al_{0.06}REE_{0.02}Sr_{0.02}Y_{0.01}Cr_{0.01}Ni_{0.01}Zn_{0.01})_{\Sigma 10.0}[(P_{3.99}Si_{1.97}S_{0.06})_{\Sigma 6.02}(O_{23.72}F_{0.23}Cl_{0.04})_{\Sigma 23.99}]$ (Table 6), or $(Ca_{8.16}Fe^{3+}_{0.76}\square_{0.74}Ti_{0.20}Al_{0.06}REE_{0.02}Sr_{0.02}Y_{0.01}Cr_{0.01}Ni_{0.01}Zn_{0.01})_{\Sigma 10.0}[(P_{4.04}Si_{1.99}S_{0.06})_{\Sigma 6.09}O_{24}](\square_{1.73}F_{0.23}Cl_{0.04})$ (not shown in Table 6) where *REE* = rare-earth elements. The absence of H_2O and CO_2 was confirmed by Raman spectroscopy. The simplified formula is $Ca_5(PO_4)_2(SiO_4)$, the same as the terrestrial orthorhombic mineral silicocarnotite (Galuskin *et al.*, 2016).

Electron microprobe analytical data for the unknown mineral referred to as silico-phosphate or calcium silico-phosphate in various volcanic and plutonic angrites have been reported by Kaneda *et al.* (2001), Mittlefehldt *et al.* (2002) and Kurat *et al.* (2004) for D'Orbigny, Jambon *et al.* (2008) for NWA 1670, Mikouchi *et al.* (2011) for NWA 4590, and Warren and Davis (1995) and Mikouchi *et al.* (2010) for Asuka 881371 (Table 6). Except for the lower formula weights probably due to the omission of trace heavy elements (mainly Sr and *REE*) in analyses, the calculated empirical formula for other measurements from D'Orbigny (Table 6; Mittlefehldt *et al.*, 2002; Kurat *et al.*, 2004; Kaneda *et al.*, 2001) are quite similar to that for tsangpoite in the present study. The 2nd datum of Mittlefehldt *et al.* (2002) with Si/P = 1 and the 4th datum with a much larger formula weight (985.6 g/mole) in Table 6 are probably due to different phase(s) or analytical artifacts. As for Ca silico-phosphates from other angrites (Table 6; Asuka 881371, Warren and Davis, 1995, Mikouchi *et al.*, 2010; NWA 1670, Jambon *et al.*, 2008; NWA 4590, Mikouchi *et al.*, 2011), except for the one measurement in NWA 1670 with lower Si/P = 0.23 and Fe^{3+}/Fe = 60% (Jambon *et al.*, 2008), the calculated formula are also closely similar to that of tsangpoite. It is clear that this unknown Ca silico-phosphate mineral commonly present in various angrites, in all probability, is tsangpoite with variable Si/P ratios and with Fe mainly in 3+ charge as was also confirmed by micro-XANES measurements on tsangpoite from NWA 4590 (Mikouchi *et al.*, 2011). Excluding the 2nd and 4th data of Mittlefehldt *et al.* (2002) in Table 6, an ~4–10% cation vacancy at the *M* site is noted for tsangpoite in various angrites. The unexpected presence of such vacancies, along with the variable Si/P ratio (0.23–0.67), explains the long existing uncertainty regarding the stoichiometry of the commonly present minor calcium silico-phosphate phase(s) in angrites; its composition was considered to be similar but not identical to nagelschmidtite $Ca_7(SiO_4)_2(PO_4)_2$ or silicocarnotite $Ca_5(PO_4)_2(SiO_4)$ (e.g. Mikouchi *et al.*, 2010) (see Discussion).

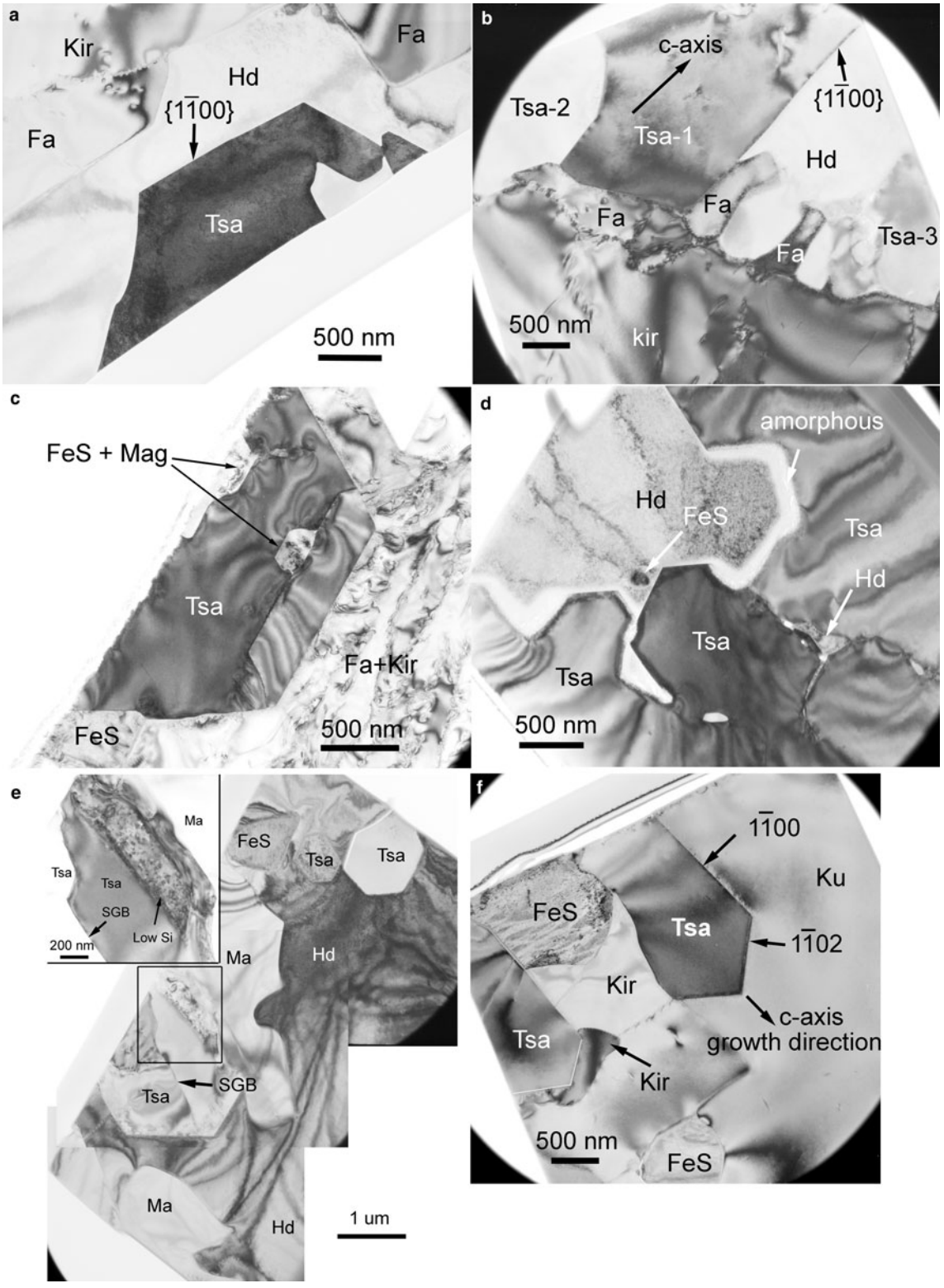

Fig. 7. TEM micrographs of tsangpoite showing (*a*) imperfect hexagonal [0001] cross-sections, (*a*,*b*) the constant presence of fayalite at the contact between tsangpoite and Fa + Kir overgrowth, (*c*) the presence of magnetite and FeS at the central tube, (*d*) the coalescence-like microstructure within the open [0001]-oriented groove filled by FeS + hedenbergite, as well as the association of (*e*) tsangpoite + matyhite (TEM section from Fig. 5f) and (*f*) tsangpoite + kuratite (TEM section from Fig. 2g). The two branches of tsangpoite grown around FeS in (*f*) are facetted by {1$\bar{1}$00} and {1$\bar{1}$02} planes. The Si-depleted thin boundary layer between tsangpoite and matyhite is shown in insert of (*e*).

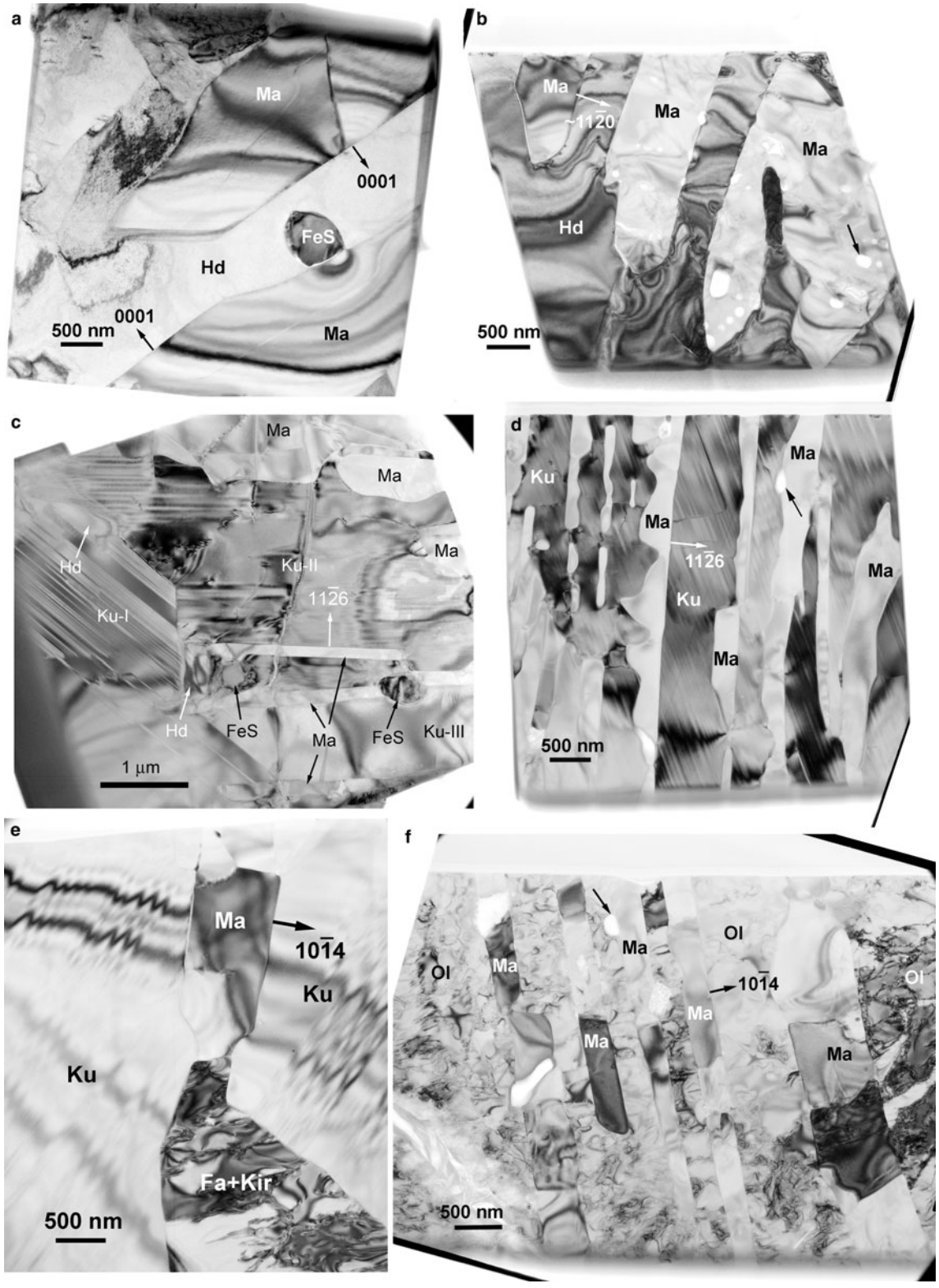

Fig. 8. TEM micrographs of matyhite dendritic plates showing: (*a*) the most commonly observed thick {0001} plates within hedenbergite; (*b*) the less commonly observed thick {11$\bar{2}$0} plates with abundant voids of various shapes within hedenbergite; (*c*) a bundle of thin ~{11$\bar{2}$6} plates with flat surfaces and associated hedenbergite + FeS embedded by multiple kuratite crystals; (*d*) a bundle of thin ~{11$\bar{2}$6} plates with very rugged surfaces and surface voids within a single kuratite crystal; (*e*) a thin ~{10$\bar{1}$4} plate of matyhite with subgrain structure enclosed by kuratite and attached to olivine at the edge; and (*f*) a bundle of thin ~{10$\bar{1}$4} plates with subgrain structure and voids within Fa + Kir symplectite. Some voids in (*b*,*d*,*f*) are indicated by arrows.

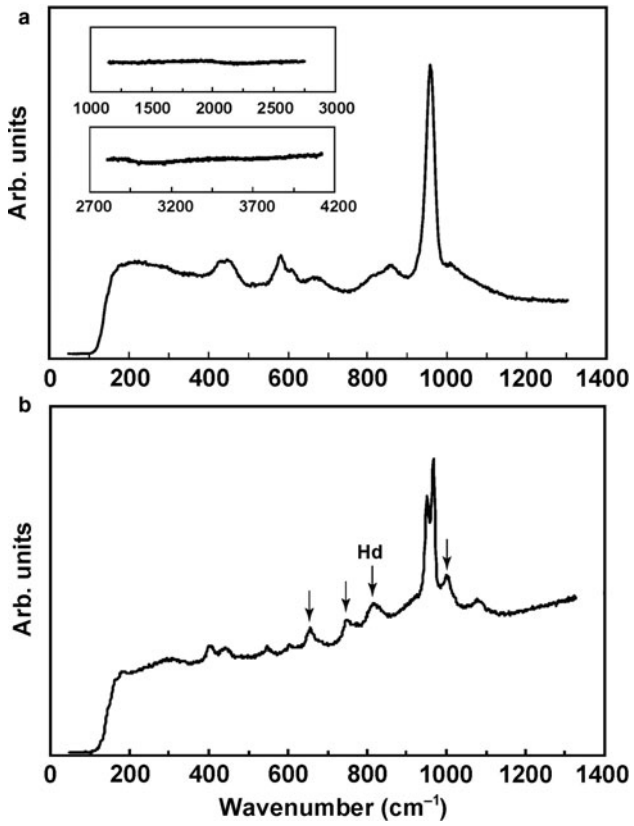

Fig. 9. Raman spectra of (*a*) tsangpoite and (*b*) matyhite with an additional peak due to the hedenbergite (Hd) matrix.

Matyhite

Due to the tiny sizes of matyhite plates, i.e. barely > 5 μm thick, it was difficult, if not impossible, to avoid interference from the matrix phase during EPMA. As the predominant hedenbergite matrix contains ~7.7 Si atoms and ~4.7 Ca atoms per 28 oxygens, it was noticed quickly that matyhite chemical data influenced by hedenbergite would readily show the sum of P + Si > 7 atoms per 28 oxygen atoms, and have the concurrent decrease in Ca. Based on these considerations, 18 analyses of matyhite with the sum of P + Si = 6.97–7.0 atoms per 28 oxygen atoms were considered acceptable and are compiled in Table 7. The lattice sites can then be assigned based on the merrillite formula $(Ca_{9-x-z}[Y,REE]_{x+z})_{\Sigma 9}Na_{1-x}(Mg,Fe,Mn)_1(P_{7-z}Si_z)_{\Sigma 7}O_{28}$, as outlined in Shearer *et al.* (2015) where *T*-site cations are P + Si = 7(0.05) for the acceptable analyses and the octahedral *M*-site cations in the decreasing order of Al→Ti→Fe^{3+}→Mg→Zn→Fe^{2+}→Mn are a total of 1. The remaining cations are assigned to the 8-fold coordinated *Ca* site in the order Fe^{2+}→Mn→Sr→*REE*, Y→Ca. This site is filled with 9 cations, and the excess Ca is then assigned to the *Na* site, along with Na and K. The empirical formula (atoms per formula unit) of the average analytical results, based on 28 oxygen atoms and 7 P + Si, is $(Ca_{8.91}Sr_{0.05}REE_{0.04})_{\Sigma 9.0}(\square_{0.52}Ca_{0.42}Na_{0.05}K_{0.01})_{\Sigma 1.0}(Fe^{2+}_{0.68}Fe^{3+}_{0.26}Al_{0.02}Ti_{0.01}Mn_{0.01}Zn_{0.01})_{\Sigma 0.99}(P_{6.75}Si_{0.26})_{\Sigma 7.01}O_{28.02}$ (with traces of Mg, Ni, Cl and S) (Table 8). The matyhite with the simplified formula $Ca_9(Ca_{0.5}o_{0.5})Fe(PO_4)_7$ having the *Na* site (6-fold coordinated irregular octahedron) half empty and half occupied by Ca and the *Mg* site (6-fold coordinated regular octahedron) fully occupied by Fe, is in fact the Fe-analogue of 'Ca-merrillite' $Ca_9(Ca_{0.5}\square_{0.5})Mg(PO_4)_7$ found in the Angra Dos Reis meteorite (Dowty, 1977) and was considered a new species in the merrillite group following the *Criteria for New Mineral Species* as detailed in Nickel and Grice (1998). The calculated empirical formula of two Fe-rich merrillites from Martian meteorites (Shearer *et al.*, 2015), and two occasional merrillite minerals from plutonic angrites (Prinz *et al.*, 1977; McKay *et al.*, 1988) are included in Table 8 for comparison.

Discussion

Relationship with other species

Tsangpoite

The comparable sets of unit-cell parameters, *d* spacings, strong reflections of tsangpoite, hydroxylapatite, and the high-temperature silico-phosphates in the binary Ca_2SiO_4–$Ca_3(PO_4)_2$ system imply that tsangpoite could be related structurally to either apatite or the high-temperature hexagonal silico-phosphates analogous to the end-member α-Ca_2SiO_4 (Tables 1 and 2). In synthetic experiments of silicate-substituted hydroxylapatite at ~1000–1200°C; i.e. $Ca_{10}(PO_4)_{6-y}(SiO_4)_y(OH)_{2-y}$, the maximum limit of Si substitution into the hexagonal apatite lattice was found to be $y = 1$–1.2 (Gomes *et al.*, 2011; Marchat *et al.*, 2013). To maintain charge neutrality, the substitution of PO_4^{3-} by SiO_4^{4-} in the hexagonal apatite lattice is accompanied by vacancy formation in the *X* site. Beyond the limit of $y = 1$–1.2, i.e. with ~50% *X* site emptied, the hexagonal structure becomes unstable (e.g. Gomes *et al.*, 2011; Marchat *et al.*, 2013 and references cited therein). A similar conclusion was reached in the dehydration experiments of hydroxylapatite, in which the space-group symmetry of partially dehydrated hydroxylapatite changes from hexagonal to triclinic when more than ~35% of the structurally bound water is removed (e.g. Alberius-Henning *et al.*, 2001 and references cited therein). In other words, the hexagonal apatite structure could be stabilised only by stuffing > ~50% OH^-, F^- or Cl^- into the *X* site. Based on these considerations, tsangpoite with the Si-enriched silicocarnotite stoichiometry, i.e. $Ca_{10}(PO_4)_4(SiO_4)_2$, might be less likely to adopt the assumed apatite-like structure, despite the rather similar reflection data. However, even with the above considerations, it is still an open question as to whether apatite-structured tsangpoite with an empty ***c*** channel could be stabilised by the abundant aliovalent cations and the charge compensating vacancies, somewhat like the volume stabilisation effect in the synthetic lead compounds $Pb_9(PO_4)_6$, $Pb_4Na(VO_4)_3$ and $Pb_8K_2(PO_4)_6$ (e.g. Dicken and Brown, 1971; Hata *et al.*, 1980; Mathew *et al.*, 1980; White and Zhili, 2003).

On the other hand, the unique structural and chemical characteristics of tsangpoite do suggest that tsangpoite is probably the high-temperature hexagonal polymorph of silicocarnotite and has its petrogenetic origin related to the 'continuous' high-temperature solid-solution phase analogous to the high-temperature α-Ca_2SiO_4 in the binary system between α-Ca_2SiO_4 (hexagonal; Mumme *et al.*, 1996) and $\bar{\alpha}$-$Ca_3(PO_4)_2$ (trigonal; Yashima and Sakai, 2003), as evidenced by the close agreement between the present electron diffraction data of tsangpoite and the XRD data of the high-*T* silico-phosphates stable at temperatures > ~1450°C (Tables 1 and 2). The existence of a continuous solid solution between two end-members of different stoichiometry and symmetry is somewhat unusual, but can be rationalised on a structural basis. In this regard, Bredig (1942, 1943) suggested that the continuous solid-solution series can be considered as

Table 5. Representative compositions (wt.%) of tsangpoite from the D'Orbigny angrite

	B2-a-2	B2-a-3	B2-a-4	B2-a-5	B2-a-6	B2-b-1	B2-b-2	B2-b-3	Average
SiO_2	14.32	12.28	12.57	11.62	10.66	13.06	12.00	13.06	12.44
TiO_2	1.88	1.58	1.83	1.52	1.88	1.50	1.44	1.60	1.66
Al_2O_3	0.63	0.23	0.28	0.25	0.26	0.23	0.30	0.32	0.31
FeO	6.67	6.24	6.09	5.33	5.32	5.36	5.04	5.46	5.69
MnO	0.04	–	0.08	0.03	0.02	–	0.08	0.02	0.03
MgO	–	–	–	–	0.03	0.05	–	–	0.01
CaO	45.84	47.72	47.27	48.12	48.31	48.24	48.06	47.40	47.62
K_2O	0.09	–	–	–	–	–	–	–	0.01
Cr_2O_3	0.08	–	0.03	0.06	–	0.07	0.06	–	0.04
NiO	0.02	–	0.13	–	0.11	–	–	0.09	0.04
P_2O_5	28.11	30.41	30.01	30.42	30.61	29.71	29.87	29.43	29.82
F	0.49	0.46	0.56	0.49	0.43	0.26	0.54	0.45	0.46
Cl	0.07	0.14	0.15	0.09	0.16	0.19	0.19	0.15	0.14
ZnO	0.27	0.01	0.04	0.20	–	0.29	0.00	0.00	0.10
SrO	0.21	0.18	0.27	0.19	0.14	0.11	0.18	0.21	0.19
Y_2O_3	0.17	0.13	0.09	0.05	0.18	0.15	0.13	0.17	0.13
La_2O_3	0.46	0.11	–	–	–	–	0.07	0.32	0.12
Pr_2O_3	0.18	0.21	0.00	0.27	0.00	0.13	–	0.34	0.14
Nd_2O_3	–	–	–	0.25	0.01	0.16	0.10	0.14	0.08
SO_3	0.44	0.52	0.47	0.43	0.53	0.48	0.39	0.39	0.46
Ce_2O_3	0.03	0.05	0.06	0.14	0.05	0.00	0.00	0.00	0.04
Total	100.00	100.27	99.93	99.46	98.70	99.99	98.45	99.55	99.53

'–' = not detected

$\bar{\alpha}$-$Ca_3(PO_4)_2$ dissolution into the hexagonal α-Ca_2SiO_4 lattice, forming the high-temperature hexagonal phase isotypic with α-K_2SO_4. Alternatively, Dickens and Brown (1971) indicated that the α-Ca_2SiO_4, $Ca_5(PO_4)_2(SiO_4)$, and $\bar{\alpha}$-$Ca_3(PO_4)_2$ phases are all related structurally to the hexagonal $K_3Na(SO_4)_2$ (aphthitalite) with certain amounts of vacant cation positions, thereby forming a continuous solid-solution series at high temperatures. The solid solution with the stoichiometry $Ca_5(PO_4)_2SiO_4$ is unquenchable, and transforms to orthorhombic silicocarnotite upon cooling at 1450°C, according to high-temperature camera measurements (see phase diagram in Nurse *et al.*, 1959 or Fix *et al.*, 1969). Except for the absence of reflections corresponding to the three largest *d* spacings of tsangpoite, the reflections from high-temperature camera powder measurements of the phase $Ca_5(PO_4)_2(SiO_4)$ at 1550°C, as well as the reflections from the quenched high-*T* phases $Ca_{11.1}(PO_4)_{1.8}(SiO_4)_{4.2}$ and $Ca_7(PO_4)_2(SiO_4)_2$ (see Table 1 and phase diagram in Nurse *et al.*, 1959) are in good agreement with those of tsangpoite determined from electron diffraction. Tsangpoite is probably structurally related to the high-*T* silico-phosphates derived from the high-*T* hexagonal α-Ca_2SiO_4 ($a = 5.53$ Å, $c = 7.31$ Å; $P6_3/mmc$) (e.g. Yamaguchi *et al.*, 1963; Table 2), as discussed below.

Given the unit-cell correspondence $a_{tsa} \approx <10\bar{1}0>_a$; $c_{tsa} \approx c_a$, tsangpoite has a triple unit-cell volume of α-Ca_2SiO_4 as outlined in the atomic projections along <0001> (see Fig. S5). Such an α-Ca_2SiO_4-derived unit cell contains 12 *M* sites and 6 *T* sites, including 2 *M*1 at (0, 0 and ½; site symmetry 6_3), 2 *M*2 at (⅔, ⅓, *z*; site symmetry 3) and (⅓, ⅔, $z + ½$; site symmetry 3), and 2 *M*3 at (⅔, ⅓, $z + ½$; site symmetry 3) and (⅓, ⅔, *z*; site symmetry 3) on three *MMM*… columns, as well as 6 *M*4 + 6 *T*1 (site symmetry 1) on six *TMTM*… columns, in accordance with the symmetry operation of the candidate $P6_3$ or $P6_3/m$ space group of tsangpoite determined by electron diffraction. Given such a space group with an ideal $Ca_{10}Si_2P_4O_{24}$ stoichiometry, tsangpoite would have a random distribution of 2 Si and 4 P at the *T*1 site. The two vacant *M* sites per unit cell can then be assigned to 2 *M*1, 2 *M*2, or 2 *M*3. The first configuration by the selective vacant 2 *M*1 results in a fully empty cation channel along the 6_3 axis. This might be energetically as unstable as the empty anion channel in the non-realistic apatite-structured tsangpoite, and therefore should be discarded. On the other hand, the second configuration by the selective vacant 2 *M*2 or 2 *M*3 is energetically more favoured to have one *M*1–*M*1…, two *M*2–□… (or two *M*3–□…), and six *T*1–*M*4… columns per unit basal area for the selective $P6_3$ space group. Only when *M*2, *M*3, *M*4 and *T*1 are all at special positions, i.e. with *m* symmetry at $z = ¼$, ¾, and all TO_4 tetrahedra are properly oriented, could tsangpoite have the alternative $P6_3/m$ space group. Note that there is a slight deviation of *M*2 or *M*3 sites (equivalent in $P6_3/mmc$) from mirror planes in the parental α-Ca_2SiO_4 structure (Mumme *et al.*, 1996). Aside from the two aforementioned 'vacant' *M* sites in the solid solution involving $\bar{\alpha}$-$Ca_3(PO_4)_2$ dissolution into the hexagonal α-Ca_2SiO_4 lattice (Bredig, 1942, 1943), there are additional 0.84 *M* vacancies per tsangpoite unit cell for charge compensation due to the substitution of aliovalent cations Ti^{4+}, Fe^{3+}, Al^{3+}, Y^{6+} and REE^{6+} for Ca^{2+}, which are therefore most probably randomly distributed throughout the tsangpoite structure.

The α-Ca_2SiO_4-derived superlattice and the cation/vacancy ordering scheme are also of concern to the structural similarity/difference between nagelschmidtite, silicocarnotite and tsangpoite. Nagelschmidtite $Ca_7□(PO_4)_2(SiO_4)_2$ with the assigned $P6_1$ space group and unit-cell correspondence $a_{nag} \approx 2a_a$, $c_{nag} \approx c_a$ (where $a_{nag} = 10.78$ Å, $c_{nag} = 21.42$ Å, $P6_1$ and $Z = 6$) (see Fig. S5) has one *MMM*… chain (6_1 axis), three equivalent *MMM*… chains (2_1 axis), six equivalent *TMTM*… chains (3_1 axis), and other two equivalent *TMTM*… chains (Widmer *et al.*, 2015). Given the $M_{42}T_{24}O_{96}$ stoichiometry deviating from 48 *M* sites and 24 *T* sites in the unit cell, nagelschmidtite requires six vacant *M* sites at different heights of the individual six equivalent *TMTM*… chains to yield six *T*□*TMTMT*□*T*… chains in accordance with the 6_1 and 3_1 symmetry of the $P6_1$ space group (see projection in fig. 8 of Widmer *et al.*, 2015). Furthermore, following the screw axis 6_1 rather than 6_3 of tsangpoite,

Table 6. Comparison of compositions (wt.%) of tsangpoite from this work and the literature in various angrites.

		D'Orbigny angrite						NWA 1670	Asuka 881371	NWA 4590	Asuka 881371
Ref.	[8]	[1]	[1]	[1]	[1]	[2]	[3]	[4]	[5]	[6]	[7]
No. analyses	8	4	2	8	6	1	1	4	19	1	1
Wt.%											
SiO_2	12.44	12.20	19.00	13.80	13.40	12.80	12.23	6.77	13.13	8.76	11.70
TiO_2	1.66	1.42	1.61	1.61	1.64	1.73	1.64	0.36	1.68	0.69	1.50
Al_2O_3	0.31	0.27	2.11	0.45	0.41	0.23	0.22	0.83	0.32	0.44	0.20
FeO	5.69	4.99	9.51	5.94	5.45	5.00	4.89	10.16	5.17	2.51	4.80
MnO	0.03	0.07	0.08	0.08	0.07	0.06	0.05	–	0.06	0.04	0.10
MgO	0.01	–	–	–	0.01	0.02	–	0.38	0.01	–	–
CaO	47.62	48.70	41.90	47.30	50.90	48.40	48.61	42.92	46.00	50.84	49.40
K_2O	0.01	–	–	–	–	–	0.01	–	0.01	–	–
Cr_2O_3	0.04	–	–	–	–	–	0.01	–	0.01	–	–
NiO	0.04	–	–	–	–	–	–	–	0.04	–	–
P_2O_5	29.82	29.70	21.90	28.10	24.50	30.70	30.50	34.39	29.50	33.96	29.40
F	0.46	–	–	–	–	–	–	0.09	–	0.00	1.00
Cl	0.14	–	–	–	–	–	–	0.07	–	0.00	0.30
ZnO	0.10	–	–	–	–	–	–	–	–	–	–
SrO	0.19	–	–	–	–	–	–	–	–	–	–
Y_2O_3	0.13	–	–	–	–	–	–	–	–	–	–
La_2O_3	0.12	–	–	–	–	–	–	–	–	–	–
Pr_2O_3	0.14	–	–	–	–	–	–	–	–	–	–
Nd_2O_3	0.08	–	–	–	–	–	–	–	–	–	–
SO_3	0.46	–	–	–	–	–	–	0.43			0.40
Ce_2O_3	0.04	–	–	–	–	–	–	–	–	–	–
Total	99.53	97.35	96.11	97.28	96.38	98.94	98.16	96.40	95.93	97.24	98.80
Atoms per formula unit											
T sites											
Si	1.967	1.974	3.094	2.231	2.281	2.024	1.955	1.105	2.134	1.412	1.876
P^{+5}	3.992	4.067	3.019	3.845	3.530	4.109	4.127	4.753	4.058	4.635	3.990
S^{+6}	0.055	–	–	–	–	–	–	0.053	–	–	0.048
M sites											
Ti	0.197	0.173	0.197	0.196	0.210	0.206	0.197	0.044	0.205	0.084	0.181
Al	0.058	0.051	0.405	0.086	0.082	0.043	0.041	0.160	0.061	0.084	0.038
Fe	0.752	0.675	1.295	0.803	0.776	0.661	0.654	1.387	0.703	0.338	0.644
Mn	0.004	0.010	0.011	0.011	0.010	0.008	0.007	–	0.008	0.005	0.014
Mg	0.002	0.000	0.000	0.000	0.003	0.005	0.000	0.092	0.002	–	–
Ca	8.069	8.440	7.310	8.191	9.282	8.200	8.324	7.507	8.009	8.782	8.485
K	0.002	–	–	–	–	–	0.002	–	0.002	–	–
Cr	0.005	–	–	–	–	–	0.001	–	0.001	–	–
Ni	0.005	–	–	–	–	–	–	–	0.005	–	–
Zn	0.012	–	–	–	–	–	–	–	–	–	–
Sr	0.017	–	–	–	–	–	–	–	–	–	–
Y	0.011	–	–	–	–	–	–	–	–	–	–
La	0.007	–	–	–	–	–	–	–	–	–	–
Pr	0.008	–	–	–	–	–	–	–	–	–	–
Nd	0.005	–	–	–	–	–	–	–	–	–	–
Ce	0.002	–	–	–	–	–	–	–	–	–	–
O, F, Cl											
O	23.72	24.0	24.0	24.0	24.0	24.0	24.0	23.95	24.0	24.0	23.46
F	0.230	–	–	–	–	–	–	0.046	–	–	0.510
Cl	0.038	–	–	–	–	–	–	0.019	–	–	0.081
Formula weight	943.6	946.2	940.3	944.7	985.6	940.0	942.7	945.0	936.7	942.0	947.0
Density	2.793										
Σ O + F + Cl	23.99	24.0	24.0	24.0	24.0	24.0	24.0	24.01	24.0	24.0	24.05
T site	6.01	6.04	6.11	6.08	5.81	6.13	6.08	5.91	6.19	6.05	5.90
M site	9.16	9.35	9.22	9.29	10.36	9.12	9.23	9.19	9.00	9.29	9.34
Si/P	0.49	0.49	1.02	0.58	0.65	0.49	0.47	0.23	0.53	0.30	0.47
Fe charge	3	3	3	3	2	3	3	2.6	3	3	3

[1] Mittlefehldt *et al.* (2002), $(Ca_{8.44}Fe^{+3}_{0.68}Ti_{0.17}Al_{0.05}Mn_{0.01}\square_{0.65})_{\Sigma 10.0}[(P_{4.07}Si_{1.97})_{\Sigma 6.04}O_{24}]$; [2] Kurat *et al.* (2004), $(Ca_{8.20}Fe^{+3}_{0.66}Ti_{0.21}Al_{0.04}Mn_{0.01}Mg_{0.01}\square_{0.87})_{\Sigma 10.0}[(P_{4.11}Si_{2.02})_{\Sigma 6.13}O_{24}]$; [3] Kaneda *et al.* (2001), $(Ca_{8.32}Fe^{+3}_{0.65}Ti_{0.20}Al_{0.04}Mn_{0.01}\square_{0.78})_{\Sigma 10.0}[(P_{4.13}Si_{1.96})_{\Sigma 6.09}O_{24}]$; [4] Jambon *et al.* (2008); [5] Warren and Davis (1995), $(Ca_{8.01}Fe^{+3}_{0.70}Ti_{0.21}Al_{0.06}Mn_{0.01}Ni_{0.01}\square_{1.0})_{\Sigma 10.0}[(P_{4.06}Si_{2.13})_{\Sigma 6.19}O_{24}]$; [6] Mikouchi *et al.* (2011), $(Ca_{8.78}Fe^{+3}_{0.34}Ti_{0.08}Al_{0.08}Mn_{0.01}\square_{0.71})_{\Sigma 10.0}[(P_{4.64}Si_{1.41})_{\Sigma 6.05}O_{24}]$; [7] Mikouchi *et al.* (2010), $(Ca_{8.49}Fe^{+3}_{0.64}Ti_{0.18}Al_{0.04}Mn_{0.01}\square_{0.68})_{\Sigma 10.0}[(P_{3.99}Si_{1.88}S_{0.05})_{\Sigma 5.92}(O_{23.46}F_{0.51}Cl_{0.08})_{\Sigma 24.05}]$; [8] this work, see Table 5.
'–' = not detected

nagelschmidtite is expected to have a *c* axis unit repetition distance three times that of tsangpoite when derived from α-Ca_2SiO_4. This is indeed the case with $c = \sim 21$ Å for nagelschmidtite and $c = \sim 7$ Å for tsangpoite. Although with much more zigzag *MMM*… or *TMTM*…. chains along the *a* axis, silicocarnotite $Ca_{10}\square(PO_4)_4(SiO_4)_2$ can be visualised as the structural derivative of α-Ca_2SiO_4 by the unit-cell correspondence $a_{sca} \approx c_a$, $b_{sca} \approx 3a_a$, $c_{sca} \approx \sqrt{3}c_a$ (where $a_{sca} = 6.72$ Å, $b_{sca} = 15.45$ Å

Table 7. Representative compositions (wt.%) of matyhite from the D'Orbigny angrite.

	D4-14	D4-15	D4-18	D4-20	D4-22	D5-26	D5-27	D5-29	D5-30	D5-49	D5-50	D5-51	D5-54	C3-61	A4-66	A4-67	A4-71	A4-73	Average
SiO_2	1.71	1.16	1.66	1.39	1.15	1.30	1.26	1.38	0.87	1.81	1.34	1.44	0.92	1.34	1.50	1.99	1.27	1.42	1.39
TiO_2	0.13	0.07	0.17	0.15	0.06	0.03	0.14	0.11	0.02	0.02	0.04	0.03	0.04	0.07	0.15	0.03	–	–	0.07
Al_2O_3	0.09	–	0.11	0.10	0.07	0.05	0.06	0.07	0.10	0.11	0.11	0.23	0.05	0.07	0.07	0.20	0.11	0.07	0.09
FeO total	6.15	6.07	6.03	6.21	6.04	6.29	6.22	6.13	6.12	6.20	6.02	5.92	6.16	5.69	5.91	6.26	6.19	6.22	6.10
MnO	–	0.02	–	–	0.04	0.09	–	0.09	0.01	0.10	0.03	–	–	0.14	–	–	0.16	–	0.04
MgO	0.03	–	0.06	0.04	–	–	–	–	0.05	–	–	–	–	–	0.04	–	–	0.03	0.01
CaO	46.24	48.36	46.90	46.76	45.25	47.22	47.57	46.38	46.94	47.22	47.32	46.96	46.44	46.49	48.20	47.31	47.51	47.98	47.06
Na_2O	0.06	–	0.10	0.05	0.11	0.10	0.08	0.25	0.12	0.34	0.03	0.11	0.01	0.11	0.24	0.42	0.49	0.10	0.15
K_2O	0.09	0.03	–	–	0.02	0.02	0.02	0.02	–	0.02	0.05	0.01	–	0.02	0.05	0.06	0.05	0.02	0.03
Cr_2O_3	–	–	0.09	–	–	–	0.03	–	–	–	–	–	–	–	0.08	0.03	0.01	–	0.01
NiO	0.14	–	–	–	–	–	–	–	–	–	–	0.10	0.03	–	–	0.08	–	–	0.02
P_2O_5	42.67	43.80	43.11	43.69	42.16	42.81	42.97	42.32	44.70	43.29	43.63	42.76	42.42	42.26	43.59	42.58	43.38	43.51	43.09
Cl	–	0.02	–	–	–	–	–	–	0.02	–	0.02	–	–	0.01	0.02	0.01	0.02	–	0.01
ZnO	0.05	–	–	0.24	–	0.03	0.07	0.26	0.02	–	–	–	–	0.09	0.11	0.00	0.02	–	0.05
SrO	0.45	0.38	0.25	0.30	0.39	0.36	0.36	0.90	0.50	0.83	0.53	0.32	0.21	0.48	0.43	0.32	0.28	0.40	0.43
La_2O_3	0.02	–	0.20	0.11	0.05	–	0.07	–	–	0.13	0.05	–	0.01	0.14	0.35	0.14	–	0.13	0.08
Nd_2O_3	0.14	0.21	0.08	0.23	–	0.16	0.18	–	0.05	0.47	0.15	0.16	0.46	0.18	0.19	0.45	–	0.21	0.18
SO_3	0.01	0.01	0.03	0.03	0.04	0.03	0.02	–	–	–	0.01	–	0.02	0.03	–	–	–	–	0.01
Ce_2O_3	0.21	0.05	0.21	0.30	0.44	0.39	0.40	0.35	0.20	0.19	0.31	0.02	0.37	0.11	0.42	0.05	0.30	0.24	0.25
Yb_2O_3	0.31	0.10	0.17	0.24	0.36	0.30	–	–	–	–	0.41	–	–	0.36	–	–	0.36	0.05	0.15
Total	98.50	100.36	99.17	99.84	96.18	99.18	99.45	98.26	100.37	100.73	100.23	98.69	97.14	99.05	101.35	99.93	100.15	100.38	99.22

'–' = not detected

and c_{sca} =10.08 Å, *Pnma* and $Z = 2$) (see Fig. S5), or be seen as a 1:1 alternation of stretched $\alpha'_{(H)}$-Ca_2SiO_4 modules (Si/P = 1), intersliced by $Ca(PO_4)^-$ modules (Galuskin *et al.*, 2016). Given that the $M_{20}T_{12}O_{48}$ stoichiometry deviates from the allowed 24 *M* sites and 12 *T* sites, silicocarnotite requires four vacant *M* sites in the unit cell. As there are six general equivalent positions for the *Pnma* space group, the four vacancies can only be placed along either two equivalent *MM*… chains or four equivalent *TMTM*… chains sitting on the {010} mirror planes ($y = ¼$ and ¾) (e.g. see projection in fig. 11 of Galuskin *et al.*, 2016). Similar to that noted in tsangpoite, the first configuration would yield an unstable configuration with two fully empty cation chains along the *a* axis, and hence should be discarded. Instead, the four vacancies have to be placed on the four individual equivalent *TMTM*… chains on the {010} mirrors, thereby yielding four *T*□*T*□*T*… chains along the *a* axis (see structural refinement in Galuskin *et al.*, 2016). In contrast to the above cases with vacancies at the specific *M* sites, the vacancies in the synthetic flamite-like phase $Ca_{15}□(PO_4)_2(SiO_4)_6$ by the unit-cell correspondence $a_{fla} \approx \sqrt{3}c_a$, $b_{fla} \approx 4a_a$, $c_{fla} \approx c_a$ (where $a_{fla} = 9.40$ Å, $b_{fla} = 21.71$ Å, $c_{fla} = 6.83$ Å, $Pnm2_1$ and $Z = 2$) were considered most likely to be placed randomly at *M2* and *M3* along *TMTM*… columns, such as Na in flamite $Ca_{14}Na_2(PO_4)_2(SiO_4)_6$ (Saalfeld and Klaska, 1981, Gfeller *et al.*, 2015; Widmer *et al.*, 2015).

In contrast to the cation–vacancy ordered structures of tsangpoite and nagelschmidtite, the high-*T* silico-phosphates in the α-Ca_2SiO_4–$\bar{\alpha}$-$Ca_3(PO_4)_2$ system most likely have the high-temperature disordered structure with all the vacancies distributed randomly in *M* sites to give the common α-Ca_2SiO_4-like unit cell with fewer reflections than tsangpoite (see Table 1). Except for the composition range ~25–40 wt.% $Ca_3(PO_4)_2$ having the high-*T* phase stability field extending down to ~<1200°C for sluggish transformation kinetics, the high-*T* silico-phosphates in the Ca_2SiO_4–$Ca_3(PO_4)_2$ system were known to be unquenchable (Nurse *et al.*, 1959; Fix *et al.*, 1969) due to high equilibrium temperatures for rather rapid phase transformation upon cooling/quenching. However, it was noted the high-*T* phase stability field of the eutectoid composition with 35 wt.% $Ca_3(PO_4)_2$ (at ~500°C) may well extend to room temperature due to the impurities (Nurse *et al.*, 1959). The impurity stabilisation effect on the high-*T* phase was also noted in the Na_2O, Fe_2O_3 and/or Al_2O_3 stabilised α-Ca_2SiO_4 solid-solution phases, which were in fact quenchable from $T > 1400$°C (Bredig, 1943; Fukuda *et al.*, 1993; see Table 2) and yet the pure α-Ca_2SiO_4 was unquenchable (Nurse *et al.*, 1959; Fix *et al.*, 1969). The time-temperature-transformation diagram of α to α'_H transition of Ca_2SiO_4 solid solution with different concentrations of foreign oxides (Na_2O, Fe_2O_3, and Al_2O_3) further showed that the kinetic cut-off temperature and the activation energy for the growth of α'_H increase steadily with increasing concentration of impurities (Fukuda *et al.*, 1993). It is thus possible that a high content of Ti^{4+}, Fe^{3+} and Al^{3+}, as tramp impurities, may extend the high-*T*-phase stability field to lower temperatures, around 1200°C, to allow vacancy ordering for tsangpoite formation, and also to avoid the high-*T* phase → silicocarnotite transformation upon cooling/quenching as reported here.

Lastly, it is emphasised that, based on the present work, tsangpoite indeed has a hexagonal crystal structure ($P6_3$ or $P6_3/m$) with a unit cell similar to apatite or the high-temperature hexagonal phase in the Ca_2SiO_4–$Ca_3(PO_4)_2$ system. Its crystal structure along with chemical composition is distinctly different from existing known mineral phases, and tsangpoite is accordingly a distinct mineral species in nature. Unfortunately, the present electron diffraction data are unable to distinguish if the tsangpoite crystal structure is more similar to an apatite structure with empty channels or to the α-Ca_2SiO_4-derived structure, nor do they clearly define the possible presence of small cation sites associated with Ti and/or Fe and the abundant structure vacancies as indicated in the empirical formula. Future single-crystal XRD studies on larger tsangpoite crystals than the tiny ones in the present study by four cycle diffractometers, coupled with further detailed spectroscopic evidence, may solve this problem.

Matyhite

Merrillite, also known as 'whitlockite' in the early literature, is one of the main Ca phosphate minerals, along with apatite, that occur

Table 8. Comparison of compositions (wt.%) of matyhite in various angrites from this work and the literature.

Ref.	D'Orbigny [4]	NWA 5789 [1]	Que 94201 A-10 [1]	Angra dos Reis [2]	LEW 86010 [3]
SiO_2	1.39	0.19	0.09	0.67	0.71
TiO_2	0.07	–	0.05	–	0.01
Al_2O_3	0.09	0.04	–	–	0.04
FeO total	6.10	5.94	6.18	1.29	1.62
MnO	0.04	0.23	0.23	–	0.04
MgO	0.01	0.92	0.36	2.82	2.68
CaO	47.06	47.07	46.64	49.40	50.68
Na_2O	0.15	0.69	0.48	0.68	–
K_2O	0.03	0.01	–	–	–
Cr_2O_3	0.01	–	–	–	–
NiO	0.02	–	–	–	–
P_2O_5	43.09	44.63	45.11	45.10	44.60
Cl	0.01	0.01	0.01	–	–
ZnO	0.05	–	–	–	–
SrO	0.43	–	–	–	–
La_2O_3	0.08	–	–	–	–
Nd_2O_3	0.18	–	–	–	–
SO_3	0.01	–	–	–	–
Ce_2O_3	0.25	–	–	–	–
Yb_2O_3	0.15	–	–	–	–
Total	99.22	99.82	99.24	99.96	100.38
Atoms per formula unit					
Ca site					
Sr	0.05				
La	0.01				
Nd	0.01				
Ce	0.02				
Y	0.01				
Ca	8.91	9.00	9.00	9.00	9.00
Σ	9.00	9.00	9.00	9.00	9.00
Mg site					
Ti	0.01	–	0.01	–	–
Al	0.02	0.01	–	–	0.01
Fe	0.94	0.91	0.95	0.19	0.24
Mn	0.01	0.04	0.04	–	0.01
Mg	–	0.25	0.10	0.76	0.72
Ni	–	–	–	–	–
Zn	0.01	–	–	–	–
Σ	0.99	1.21	1.09	0.95	0.98
Na site		–	–	–	–
Ca	0.42	0.26	0.14	0.52	0.77
Na	0.05	0.25	0.17	0.24	–
K	0.01	–	–	–	–
Σ	0.48	0.51	0.31	0.76	0.77
P site					
P^{5+}	6.75	6.94	6.98	6.87	6.80
Si	0.26	0.03	0.02	0.12	0.13
Σ	7.01	6.97	7.00	6.99	6.92
Σ O	28.02	28.00	28.00	28.00	28.00
Formula weight	1103.5	1100.5	1090.0	1084.4	1085.4
Density	2.992				
Fe charge	2.28	2.00	2.40	2.00	2.00

[1] Martian meteorites (Shearer *et al.*, 2015), $Ca_9(\square_{0.49}Ca_{0.26}Na_{0.25})_{\Sigma1.0}(Fe^{2+}_{0.91}Mn_{0.04}Al_{0.01}Mg_{0.25})_{\Sigma1.21}(P_{6.94}Si_{0.03})_{\Sigma6.97}O_{28}$ or $Ca_9(\square_{0.69}Na_{0.17}Ca_{0.14})_{\Sigma1.0}(Fe^{2+}_{0.57}Fe^{3+}_{0.38}Mg_{0.10}Mn_{0.04}Ti_{0.01})_{\Sigma1.09}(P_{6.98}Si_{0.02})_{\Sigma7.0}O_{28}$; [2] plutonic angrite, including 0.01% Y_2O_3 and 0.25% Ce_2O_3 (Prinz *et al.*, 1977), $Ca_9(Ca_{0.52}Na_{0.24}\square_{0.24})_{\Sigma1.0}(Mg_{0.76}Fe^{2+}_{0.19})_{\Sigma0.95}(P_{6.87}Si_{0.12})_{\Sigma6.99}O_{28}$; [3] plutonic angrite (Mckay *et al.*, 1988), $Ca_9(Ca_{0.77}\square_{0.23})_{\Sigma1.0}(Mg_{0.72}Fe^{2+}_{0.24}Al_{0.01}Mn_{0.01})_{\Sigma0.98}(P_{6.80}Si_{0.13})_{\Sigma6.92}O_{28}$; [4] this work, see Table 7.
'–' = not detected

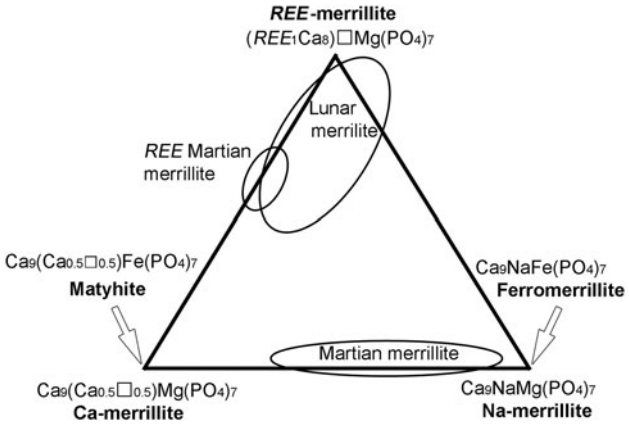

Fig. 10. Ternary diagram illustrating the composition variations of extra-terrestrial merrillites versus Ca-merrillite, matyhite, Na-merrillite, ferromerrillite, and *REE*-merrillite (modified from fig. 7 in Shearer *et al.*, 2015).

mainly in Martian meteorites and Lunar rocks, and rarely in terrestrial pyrometamorphic rocks (e.g. Galuskina *et al.*, 2016). Significant structural differences between terrestrial whitlockite $Ca_9Mg(PO_4)_6(PO_3OH)$ and the extra-terrestrial merrillite $Ca_9NaMg(PO_4)_7$, e.g. the split of the *P*1 site in merrillite into *P*(A) and *P*(A') sites and the consequent inversion of the *P*(A) tetrahedron with incorporation of hydrogen atoms in whitlockite (e.g. Gopal and Calvo, 1972; Dowty, 1977; Yashima *et al.*, 2003; Hughes *et al.*, 2006, Jolliff *et al.*, 2006; Hughes *et al.*, 2008), suggest that they are in fact two different minerals and the exclusive usage of 'merrillite' for the hydrogen-free extra-terrestrial varieties is warranted (Dowty, 1977; Rubin, 1997). Not considering the limited substitution of Si for P at tetrahedral sites, the compositions of extra-terrestrial merrillite varieties can be described by the general formula $(Ca_{9-x-z}[Y,REE]_{x+z})_{\Sigma9}Na_{1-x}(Mg,Fe,Mn)_{\Sigma1}(P_{7-z}Si_z)_{\Sigma7}O_{28}$, and can be plotted in a ternary diagram: Ca-merrillite $Ca_9(Ca_{0.5}\square_{0.5})(Mg,Fe,Mn)_{\Sigma1}(PO_4)_7$, Na-merrillite $Ca_9Na(Mg,Fe,Mn)_{\Sigma1}(PO_4)_7$ [i.e. 'merrillite', approved by the International Mineralogical Association (IMA) in 1977] and *REE*-merrillite $(Ca_8[Y,REE]_1)\square(Mg,Fe,Mn)_{\Sigma1}(PO_4)_7$ (see Fig. 10 modified from fig. 7 in Shearer *et al.*, 2015) (e.g. Dowty, 1977; Jolliff *et al.*, 2006; Shearer *et al.*, 2015). As ferromerrillite $Ca_9NaFe(PO_4)_7$ from the Shergotty meteorite has been considered as the Fe-analogue of Na-merrillite $Ca_9NaMg(PO_4)_7$ and approved as a new merrillite-group mineral by the IMA (Britvin *et al.*, 2016; IMA2006-039), the present matyhite $Ca_9(Ca_{0.5}\square_{0.5})Fe(PO_4)_7$ with the *Na* site (irregular 6-fold coordinated in merrillite structure) half empty and half occupied by Ca and the *Mg* site (regular 6-fold coordinated in merrillite structure) fully occupied by Fe, is in fact the Fe-analogue of Ca-merrillite $Ca_9(Ca_{0.5}\square_{0.5})Mg(PO_4)_7$ and should therefore be considered as a new species in the merrillite group, following the *Criteria for New Mineral Species* as detailed in Nickel and Grice (1998).

The chemical variations among merrillites in Martian meteorites, Lunar rocks, and the D'Orbigny angrite can be illustrated using the Ca-merrillite, Na-merrillite and *REE*-merrillite ternary diagram (see Fig. 10 modified from fig. 7 in Shearer *et al.*, 2015). Due to low abundance in *REE*, the Martian merrillites mostly lie along the Ca-merrillite–Na-merrillite join, and are dominated by the coupled substitution $Ca_{Na\text{-}site} + \square_{Na\text{-}site} \Leftrightarrow 2Na_{Na\text{-}site}$. In contrast to the Martian merrillites, Lunar merrillites have a large *REE*-merrillite component, and are therefore displaced from the Ca-merrillite–Na-merrillite join towards the *REE*-merrillite apex. Among all extra-terrestrial merrillites, matyhite has the greatest Ca, Fe and Si abundances, i.e. 9.33 Ca atoms, 0.94 Fe atoms and 0.26 Si atoms per 28 oxygen atoms (Table 8), and appears to be a rather rare mineral species in

terms of composition. Among the ample chemical data of Fe-rich merrillite minerals from Martian meteorites in Shearer *et al.* (2015), there are only two analyses having similar *Na*-site occupancies with Ca > Na + K, comparable to matyhite (see Table 8). As for the occasional merrillite minerals from plutonic angrites, their Mg-, Ca- and Na-site occupancies are closer to Ca-merrillite (Prinz *et al.*, 1977; McKay *et al.*, 1988) (see Table 8).

The formation of tsangpoite, matyhite and kuratite in the D'Orbigny angrite

Aside from the debate on the possible non-igneous origin of the D'Orbigny angrite (Mittlefehldt *et al.*, 2002; Kurat *et al.*, 2004; Varela *et al.*, 2005; 2017), angrites are usually considered to be basaltic igneous rocks. Following the igneous scenario, the accessory minerals kuratite, matyhite and tsangpoite, along with Al–Ti-bearing hedenbergite, troilite, and Ca and Fe-rich olivine, are considered as mesostasis phases crystallised from residue magmas (e.g. Mittlefehldt *et al.*, 2002; Keil, 2012), similar to the sequential crystallisation of merrillite and apatite from magma in Martian meteorites and/or Lunar rocks (e.g. Greenwood *et al.*, 2003; Gross *et al.*, 2013), or the formation of Fe^{2+}-dominant rhönites in terrestrial undersaturated basaltic rocks (Gamble and Kyle, 1987; Grapes and Keller, 2010; Havette *et al.*, 1982; Olsson, 1983). In accordance with the above, the occurrence of kuratite, matyhite and tsangpoite embedded in hedenbergite or the Ca-rich fayalite + kirschsteinite intergrowth rim of resorbed Fe sulfide suggests that these phases could have crystallised from an interstitial melt at a very late stage of rock formation. This interstitial melt must be subsilicic, almost Mg-, Na- and K-free but enriched in Ca, Fe, Ti, Al and P.

Alternatively, the close petrographic relations between tsangpoite/matyhite and the resorbed Fe sulfide rimed by the Fa + Kir symplectite, such as: (1) the nucleation of tsangpoite with magnetite ± other phases as inclusions in the local partial melting-like domain in 'intact' Fe sulfide (Fig. 2*a–c*) or at the core of resorbed Fe sulfide (Fig. 5*a*); (2) the elongated tsangpoite crystal extending outward from the core of an Fe sulfide grain into hedenbergite (Figs 3*f*, 5*c*); (3) the commonly observed bundles of sub-parallel, elongated tsangpoite crystals growing from the Fa + Kir symplectic rim of Fe sulfide outward into hedenbergite (see Figs 1*a*,*b*, 3*b*,*c*); and (4) sets of dendritic matyhite plates subparallel within the Fa + Kir symplectic rim of Fe sulfide extending outward into hedenbergite (Figs 1*d*, 4*d*,*e*); would infer that these new minerals probably represent metasomatic products resulting from reactions between an intruding Ca–Ti–Al–P–O-rich metasomatic agent, which could be a secondary melt (as suggested in Mittlefehldt *et al.*, 2002), a liquid or gas, and the porous olivine–plagioclase plate + Fa–Kir overgrowth (over olivine) + augite + Fe sulfide aggregates, similar to the formation process proposed for kuratite (Hwang *et al.*, 2016*a*) and in accordance with the non-igneous genetic processes of the D'Orbigny angrite proposed by Kurat *et al.* (2004) and Varela *et al.* (2003). In either case, the formation sequence is probably tsangpoite → matyhite → kuratite → Fa + Kir symplectite (over resorbed Fe sulfide) → hedenbergite, according to petrogenetic relationships, and the crystallisation temperatures must be >1000°C, considering the: co-presence of Ca-rich fayalite and kirschsteinite (Mukhopadhyay and Lindsley, 1983; Sokol *et al.*, 2002); the stabilisation of the ordered tsangpoite structure by Fe_2O_3 and Al_2O_3 at ~1200°C (this study); the partial melting of Fe sulfide at ~1200°C (Ehfers, 1972) as evidenced by the FeS droplets in matyhite plates (Fig. 4*c–f*); and the 950–1180°C stability field of rhönites based on the available experimental (Kunzmann, 1999) and empirical (e.g. Grapes and Keller, 2010; Sharygin *et al.*, 2011; Peretyazhko *et al.*, 2017) observations.

Whereas the above scenarios rationalise the occurrences of euhedral tsangpoite, matyhite and kuratite in D'Orbigny, some issues regarding the formation mechanisms/conditions of these new minerals require further consideration/investigation. First of all, unless it was due to the extreme Fe^{3+} partition in tsangpoite involving unknown kinetics problems, the very high $Fe^{3+}/\Sigma Fe$ ratio (~1) of tsangpoite (this study; Mikouchi *et al.*, 2011), compared to the values of ~0.3, ~0.05 and ~0.15, respectively, for matyhite (this study), kuratite (Hwang *et al.*, 2016*a*) and ulvöspinel (see Table S1*b* from Mittlefehldt *et al.*, 2002), might reflect the change in f_{O_2} during crystallisation of grain-boundary phases in D'Orbigny. However, without proper temperature constraints, it is hard to address this issue further. Besides, unlike the common merrillite–apatite intergrowths due to sequential crystallisation in Martian magma (e.g. Greenwood *et al.*, 2003; Gross *et al.*, 2013), tsangpoite and matyhite occur exclusively in different hedenbergite domains at the contact with Fa–Kir intergrowths. Unless by melt immiscibility similar to that in calc-alkali phosphate–silicate systems (e.g. Toropov *et al.*, 1972; Rabinovich *et al.*, 1980) or some unknown causes, it is hard to envision how the composition of a melt phase could vary so greatly that two phosphate minerals of different compositions and structures would separately crystallise at different domains in the residue melt. Further study is also required to clarify how a crystallisation/growth process could possibly yield the elongated tsangpoite crystal with the characteristic, continuous central microtube filled by magnetite + ferrite + Fe–S–O (Figs 1*c*, 3*e*,*f*), and with the pronounced bimodal crystal sizes as illustrated in Fig. 2*d–i*.

Concluding remarks

Two new minerals: tsangpoite (silicate–phosphate) and matyhite (phosphate), mainly in association with kuratite, ulvöspinel, hedenbergite, Ca and Fe olivine, and Fe sulfide were identified in the D'Orbigny angrite meteorite, a possible analogue of terrestrial dolerite/diabase in texture. The kuratite and matyhite, along with kuratite, occurred as idiomorphic crystals in the marginal part of hedenbergite or in the Fa–Kir symplectite associated with Fe sulfide indicating they were probably crystallised from a residue melt. Alternatively, texture observations, especially petrographic relationships between the new minerals, Fe sulfide and Fa–Kir symplectite, point to a possible origin of these minerals from metasomatic reactions between an intruding Ca–Fe–Ti–Al–P–O-rich agent and the porous olivine-plagioclase plate + Fa–Kir overgrowth + augite + Fe sulfide aggregates, similar to the formation process of kuratite proposed by Hwang *et al.* (2016*a*), or the genetic processes of D'Orbigny proposed by Kurat *et al.* (2004) and Varela *et al.* (2003). The unique compositions of these new minerals truly reflect the high Ca, Fe, Ti and Al, as well as the low Mg, K and Na chemical characteristics of the angrite parent body.

Supplementary material. To view supplementary material for this article, please visit https://doi.org/10.1180/mgm.2018.125

Acknowledgements. This research is supported by funding from MOST, Taiwan, Republic of China. Helpful suggestions and comments by reviewers are highly appreciated. We thank in particular E.V. Galuskin for pointing out the structure ambiguity of tsangpoite to be solved in future work.

References

Alberius-Henning P., Adolfsson E., Grins J. and Fitch A. (2001) Triclinic oxyhydroxyapatite. *Journal of Materials Science*, **36**, 663–668.

Britvin S.N., Krivovichev S.V. and Armbruster T. (2016) Ferromerrillite, $Ca_9NaFe^{2+}(PO_4)_7$, a new mineral from the Martian meteorites, and some insights into merrillite-tuite transformation in shergottites. *European Journal of Mineralogy*, **28**, 125–136.

Bredig M.A. (1942) Isomorphism and allotropy in compounds of the type A_2XO_4. *Journal of Chemical Physics*, **46**, 747–764.

Bredig M.A. (1943) Phase relations in the system calcium orthosilicate-orthophosphate. *American Mineralogist*, **28**, 594–601.

de Aza P. N., Santos C., Pazo A., de Aza S., Cuscó R. and Artús L. (1997) Vibrational properties of calcium phosphate compounds. 1. Raman spectrum of β-tricalcium phosphate. *Chemistry of Materials*, **9**, 912–915.

Dickens B. and Brown W.E. (1971) The crystal structure of $Ca_5(PO_4)_2SiO_4$ (silico-carnotite). *Tschermaks Mineralogische und Petrographische Mitteilungen*, **16**, 1–27.

Dickens B., Schroeder L.W. and Brown W.E. (1974) Crystallographic studies of the role of Mg as a stabilizing impurity in β-$Ca_3(PO_4)_2$. *Journal of Solid State Chemistry*, **10**, 232–248.

Dowty E. (1977) Phosphate in Angra dos Reis: structure and composition of the $Ca_3(PO_4)_2$ minerals. *Earth and Planetary Science Letters*, **35**, 347–351.

Ehfers E.G. (1972) *The Interpretation of Geological Phase Diagrams*. W.H. Freeman and Co., Ltd., San Francisco, USA, 280 pp.

Fix W., Heymann H. and Heinke R. (1969) Subsolidus relations in the system $2CaOSiO_2$–$3CaOP_2O_5$. *Journal of American Ceramics Society*, **52**, 346–347.

Fukuda K., Maki I., Toyoda K. and Ito S. (1993) Kinetics of the α-to-α′$_H$ polymorphic phase transition of Ca_2SiO_4 solid solutions. *Journal of American Ceramics Society*, **76**, 1821–1824.

Fukuda K., Maki I., Ito S. and Miyake T. (1997) Structural change in phosphorus-bearing dicalcium silicates. *Journal of Ceramic Society of Japan*, **105**, 117–121.

Galuskin E.V., Galuskina I.O., Gfeller F., Krüger B., Kusz J., Vapnik Y., Dulski M. and Dzierżanowski P. (2016) Silicocarnotite, $Ca_5[(SiO_4)(PO_4)](PO_4)$, a new 'old' mineral from the Negev Desert, Israel, and the ternesite-silicocarnotite solid solution: indicators of high-temperature alteration of pyrometamorphic rocks of the Hatrurim Complex, Southern Levant. *European Journal of Mineralogy*, **28**, 105–112.

Galuskina I.O., Galuskin E.V. and Vapnik Y.A. (2016) Terrestrial merrillite. 2nd European Mineralogy Conference. *Plinius*, **42**, 563 [abstract].

Gamble J.A. and Kyle P.R. (1987) The origins of glass and amphibole in spinel-wehrlite xenoliths from Foster Crater, McMurdo Volcanic Group, Antarctica. *Journal of Petrology*, **28**, 755–779.

Gfeller F., Widmer R., Krüger B., Galuskin I.O. and Armbruster T. (2015) The crystal structure of flamite and its relation to Ca_2SiO_4 polymorphs and nagelschmidtite. *European Journal of Mineralogy*, **27**, 755–769.

Gomes S., Nedelec J.M., Jallot E. and Sheptyakov D. (2011) Silicon location in silicate-substituted calcium phosphate ceramics determined by neutron diffraction. *Crystal Growth and Designs*, **11**, 4017–4026.

Goodrich C.A. (1988) Petrology of the unique achondrite LEW 86010. *19th Lunar and Planetary Science Conference*, abstract #1201, 399–400. [Lunar and Planetary Institute abstracts available at https://www.lpi.usra.edu/publications/absearch/]

Gopal R. and Calvo C. (1972) Structure relationship of whitlockite and β-$Ca_3(PO_4)_2$. *Nature Physical Science*, **237**, 30–32.

Grapes R. and Keller J. (2010) Fe^{2+}-dominant rhönite in undersaturated alkaline basaltic rocks, Kaiserstuhl volcanic complex, Upper Rhine Graben, SW Germany. *European Journal of Mineralogy*, **22**, 285–292.

Greenwood J.P., Blake R.E. and Coath C.D. (2003) Ion microprobe measurements of $^{18}O/^{16}O$ ratios of phosphate minerals in the Martian meteorites ALH84001 and Los Angeles. *Geochimica et Cosmochimica Acta*, **67**, 2289–2298.

Gross J., Filiberto J., Herd C.D.K., Melwani Daswani M., Schwenzer S.P. and Treiman A.H. (2013) Petrography, mineral chemistry, and crystallization history of olivine-phyric shergottite NWA 6234: a new melt composition. *Meteoritics & Planetary Science*, **48**, 854–871.

Hata M., Marumo F., Iwai S. and Aoki H. (1980) Structure of a lead apatite $Pb_9(PO_4)$. *Acta Crystallographica*, **B36**, 2128–2130.

Havette A., Clocchiatti R., Nativel P. and Montaggioni L.F. (1982) Une paragenèse inhabituelle à fassaïte, mélilite et rhönite dans un basalte alcalin contaminé au contact d'un récif coralline (Saint-Leu, Ile de la Réunion). *Bulletin de Minéralogie*, **105**, 364–375.

Hughes J.M., Jolliff B.L. and Gunter M.E. (2006) The atomic arrangement of merrillite from the Fra Mauro Formation, Apollo 14 Lunar mission: The first structure of merrillite from the Moon. *American Mineralogist*, **91**, 1547–1595.

Hughes J.M., Jolliff B.L. and Rakovan J. (2008) The crystal chemistry of whitlockite and merrillite and the dehydrogenation of whitlockite to merrillite. *American Mineralogist*, **93**, 1300–1305.

Hwang S.L., Shen P., Chu H.T., Yui T.F., Varela M.,E. and Iizuka Y. (2015) Tsangpoite, IMA 2014-110. CNMNC Newsletter No. 25. *Mineralogical Magazine*, **79**, 529–535.

Hwang S.L., Shen P., Chu H.T., Yui T.F., Varela M.E. and Iizuka Y. (2016*a*) Kuratite, $Ca_4(Fe^{2+}_{10}Ti_2)O_4[Si_8Al_4O_{36}]$, the Fe^{2+}-analogue of rhönite, a new mineral from the D'Orbigny angrite meteorite. *Mineralogical Magazine*, **80**, 1067–1076.

Hwang S.L., Shen P., Chu H.T., Yui T.F., Varela M.E. and Iizuka Y. (2016*b*) Matyhite, IMA 2015-121. CNMNC Newsletter No. 31. *Mineralogical Magazine*, **80**, 691–697.

Ibáñez J., Artús L., Cuscó R., López Á., Menéndez E. and Andrade M.C. (2007) Hydration and carbonation of monoclinic C2S and C3S studied by Raman spectroscopy. *Journal of Raman Spectroscopy*, **38**, 61–67.

Jambon A., Barrat J.-A., Boudouma O., Fonteilles M., Badia D., Göpel C. and Bohn M. (2005) Mineralogy and petrology of the angrite Northwest Africa 1296. *Meteoritics & Planetary Science*, **40**, 361–375.

Jambon A., Boudouma O., Fonteilles M., Le Guillou C., Badia D. and Barrat J.A. (2008) Petrology and mineralogy of the angrite Northwest Africa 1670. *Meteoritics & Planetary Science*, **43**, 1783–1795.

Jambon A. and Boudouma O. (2011) Evidence for rhönite in angrites D'Orbigny and Sahara 99555. *74th Annual Meteoritical Society Meeting*, abstract #5167. [Lunar and Planetary Institute abstracts available at https://www.lpi.usra.edu/publications/absearch/]

Jillavenkatesa A. and Condrate Sr. R.A. (1998) The infrared and Raman spectra of β-and α-tricalcium phosphate $Ca_3(PO_4)_2$. *Spectroscopy Letters*, **31**, 1619–1634.

Jolliff B.L., Hughes J.M., Freeman J.J. and Zeigler R.A. (2006) Crystal chemistry of Lunar merrillite and comparison to other meteoritic and planetary suites of whitlockite and merrillite. *American Mineralogist*, **91**, 1583–1595.

Kaneda K., Mikouchi T., Saito A., Sugiyama K., Ohsumi K., Mukai M., Osaka T., Miyata Y., Nakai M., Kasama T., Chikami J. and Miyamoto M. (2001) Mineralogy of unique calcium silico-phosphates in angrites. *32nd Lunar and Planetary Science Conference*, abstract #2127. [Lunar and Planetary Institute abstracts available at https://www.lpi.usra.edu/publications/absearch/].

Keil K. (2012) Angrites, a small but diverse suite of ancient, silica-undersaturated volcanic-plutonic mafic meteorites, and the history of their parent asteroid. *Chemie der Erde – Geochemistry*, **72**, 191–218.

Kunzmann T. (1999) The aenigmatite-rhönite mineral group. *European Journal of Mineralogy*, **11**, 743–756.

Kurat G., Varela M.E., Brandstätter F., Weckwerth G., Clayton R., Weber H.W., Schultz L., Wäsch E. and Nazarov M.A. (2004) D'Orbigny: A non-igneous angritic achondrite? *Geochiica et Cosmochimica Acta*, **68**, 1901–1921.

Lugo G.J., Mazón P., Baudin C. and de Aza P.N. (2015) Nurse's A-phase: synthesis and characterization in the binary system Ca_2SiO_4-$Ca_3(PO_4)_2$. *Journal of American Ceramics Society*, **98**, 3042–3046.

Marchat D., Zymelka M., Coelho C., Gremillard L., Joly-Pottuz L., Babonneau F., Esnouf C., Chevalier J. and Bernache-Assollant D. (2013) Accurate characterization of pure silicon-substituted hydroxyapatite powders synthesized by a new precipitation route. *Acta Biomaterialia*, **9**, 6992–7004.

Mathew M., Brown W.E., Austin M. and Negas T. (1980) Lead alkali apatites without hexad anion: The crystal structure of $Pb_8K_2(PO_4)_6$. *Journal of Solid State Chemistry*, **35**, 69–76.

McKay G., Lindstrom D., Yang S.R. and Wagstaff J. (1988) Petrology of unique achondrite Lewis Cliff 86010. *19th Lunar and Planetary Science Conference*,

abstract #1385, 762–763. [Lunar and Planetary Institute abstracts available at https://www.lpi.usra.edu/publications/absearch/].

McKay G., Crozaz G., Wagstaff J., Yang S.R. and Lundberg L. (1990) A petrographic, electron microprobe and ion probe study of mini-angrite Lewis Cliff887051. *19th Lunar and Planetary Science Conference*, abstract #1393, 771–772. [Lunar and Planetary Institute abstracts available at https://www.lpi.usra.edu/publications/absearch/].

Mikouchi T. and McKay G. (2001) Mineralogical investigation of D'Orbigny: A new angrite showing close affinities to Asuka 881371, Sahara 99555 and Lewis Cliff 87051. *32nd Lunar and Planetary Science Conference*, abstract #1876. [Lunar and Planetary Institute abstracts available at https://www.lpi.usra.edu/publications/absearch/].

Mikouchi T., Miyamoto M. and McKay G. (1996) Mineralogy study of angrite Asuka-881371: Its possible relation to angrite LEW 87051 (abstract). *Antarctic Meteorites*, **9**, 174–188.

Mikouchi T., Kaneda K., Miyamoto M., Sugiyama K. and Ohsumi K. (2001) Micro Raman spectroscopy of unknown calcium silico-phosphates in angrite meteorites.. *11th V. M. Goldschmidt Conference*, abstract #3659.

Mikouchi T., Sugiyama K., Kato Y., Yamaguchi A., Koizumi E. and Kaneda K. (2010) Mineralogy of calcium silico-phosphates in angrites compared with related phases in heated eucrite and synthetic analog. *41st Lunar and Planetary Science Conference*, abstract #2343. [Lunar and Planetary Institute abstracts available at https://www.lpi.usra.edu/publications/absearch/].

Mikouchi T., Sugiyama K., Satake W. and Amelin Y. (2011) Mineralogy and crystallography of calcium silico-phosphate in Northwest Africa 4590 angrite.. *42nd Lunar and Planetary Science Conference*, abstract #2026. [Lunar and Planetary Institute abstracts available at https://www.lpi.usra.edu/publications/absearch/].

Mittlefehldt D.W. and Lindstrom M.M. (1990) Geochemistry and genesis of angrites. *Geochimica et. Cosmochimica Acta*, **54**, 3209–3218.

Mittlefehldt D.W., Killgore M. and Lee M.T. (2002) Petrology and geochemistry of D'Orbigny, geochemistry of Sahara 99555, and the origins of angrites. *Meteoritics & Planetary Science*, **37**, 345–369.

Mukhopadhyay D.K. and Lindsley D.H. (1983) Phase relations in the join kirschsteinite ($CaFeSiO_4$)-fayalite (Fe_2SiO_4). *American Mineralogist*, **68**, 1089–1094.

Mumme W.G., Cranswick L. and Chakoumakos B. (1996) Rietveld crystal structure refinements from high temperature neutron powder diffraction data for the polymorphs of dicalcium silicate. *Neues Jahrbuch für Mineralogie-Abhandlungen*, **170**, 171–188.

Nickel E.H. and Grice J.D. (1998) The IMA Commission on New Minerals and Mineral Names: procedures and guidelines on mineral nomenclature. *The Canadian Mineralogist*, **36**, 913–926.

Nurse R.W., Welch J.H. and Gutt W. (1959) High-temperature phase equilibria in the system dicalcium silicate-tricalcium phosphate. *Journal of the Chemical Society*, **1959**, 1077–1083.

Olsson H.B. (1983) Rhönite from Skåne (Scania), southern Sweden. *Geologiska Föreningen i Stockholm Förhandlingar*, **105**, 281–286.

Peretyazhko I.S., Savina E.A. and Khromova E.A. (2017) Minerals of the rhönite-kuratite series in paralavas from a new combustion metamorphic complex in the Choir-Nyalga basin (Central Mongolia): Composition, mineral assemblages and formation conditions. *Mineralogical Magazine*, **81**, 949–974.

Prinz M. and Weisberg M.K. (1995) Asuka 881371 and the angrites: Origin in a heterogeneous, CAI-enriched, differentiated, volatile depleted body (abstract) *Antarctic Meteorites*, **20**, 207–210.

Prinz M., Keil K., Hlava P.F., Berkley J.L., Gomes C.B. and Curvello W.S. (1977) Studies of Brazilian Meteorites, III. Origin and history of the Angra dos Reis achondrite. *Earth and Planetary Science Letters*, **35**, 317–330.

Rabadan-Ros R., Velásquez P.A., Meseguer-Olmo L. and de Aza P.N. (2016) Morphological and Structural Study of a Novel Porous Nurse's A Ceramic with Osteoconductive Properties for Tissue Engineering. *Materials* (*Basel*), **9**, 474–487.

Rabinovich E.M., Ish-Shalom M. and Kisilev A. (1980) Metastable liquid immiscibility and Vycor-type glass in phosphate-silicate systems. *Journal of Materials Science*, **15**, 2027–2038.

Rubin A.E. (1997) Mineralogy of meteorite groups: An update. *Meteoritics & Planetary Science*, **32**, 733–734.

Rubin A.E. and Ma C. (2017) Meteoritic minerals and their origins. *Chemie der Erde – Geochemistry*, **77**, 325–385.

Saalfeld H. and Klaska K.H. (1981) The crystal structure of $6Ca_2SiO_4$-$1Ca_3(PO_4)$. *Zeitschrift für Kristallographie-Crystalline Materials*, **155**, 65–73.

Serena S., Sainz M.A. and Caballero A. (2014) Single-phase silicocarnotite synthesis in the subsystem $Ca_3(PO_4)_2$–Ca_2SiO_4. *Ceramics International*, **40**, 8245–8252.

Serena S., Caballero A., de Aza P.N. and Sainz M.A. (2015) New evaluation of the in vitro response of silicocarnotite monophasic material. *Ceramics International*, **41**, 9411–9419.

Sharygin V.V., Kthay K., Szab C., Timina T.J., Trk K., Vapnik Y. and Kuzmin D.V. (2011) Rhönite in alkali basalts: Silicate melt inclusions in olivine phenocrysts. *Russian Geology and Geophysics*, **52**, 1334–1352.

Shearer C.K., Burger P.V., Papike J.J., McCubbin F.M. and Bell A.S. (2015) Crystal chemistry of merrillite from Martian meteorites: Mineralogical recorders of magmatic processes and planetary differentiation. *Meteoritics & Planetary Science*, **50**, 649–673.

Sokol E., Sharygin V., Kalugin V., Volkova N. and Nigmatulina E. (2002) Fayalite and kirschsteinite solid solutions in melts from burned spoil-heaps, South Urals, Russia. *European Journal of Mineralogy*, **14**, 795–807.

Toropov N.A., Barzakovskiv V.P., Lapin V.V., Kurtseva N.N. and Baykova A.I. (1972) *Pp*. 298–311 in: *Diagrammy Sostoyaniya Silikatnykj Sistem* (*Phase Diagrams of Silicate Systems*). Nauka, Leningrad.

Varela M.E., Kurat G., Zinner E., Métrich N., Brandstätter F., Ntaflos T. and Sylvester P. (2003) Glasses in D'Orbigny angrite. *Geochimica et Cosmochimica Acta*, **67**, 5027–5046.

Varela M.E., Kurat G., Zinner E., Hoppe P., Ntaflos T. and Nazarov M.A. (2005) The non-igneous genesis of angrites: Support from trace element distribution between phases in D'Orbigny. *Meteoritics & Planetary Science*, **40**, 409–430.

Varela M.E., Hwang S.L., Shen P., Chu H.T., Yui T.F., Iizuka Y., Brandstätter F. and Abdu Y.A. (2017) Olivinites in the angrites D' Orbigny: Vestiges of the pristine reducing conditions during angrites formation. *Geochimica et Cosmochimica Acta*, **217**, 349–364.

Warren P.H. and Davis A.M. (1995) Consortium investigation of the Asuka 881371 angrite: petrographic, electron microprobe and ion microprobe observations (abstract). *Antarctic Meteorites*, **20**, 257–260.

White T.J. and Zhili D. (2003) Structural derivation and crystal chemistry of apatites. *Acta Crystallographica*, **B59**, 1–16.

Whitney D.L. and Evans B.W. (2010) Abbreviations for names of rock-forming minerals. *American Mineralogist*, **95**, 185–187.

Widmer R., Gfeller F. and Armbruster T. (2015) Structural and crystal chemical investigation of intermediate phases in the system Ca_2SiO_4–$Ca_3(PO_4)_2$–$CaNaPO_4$. *Journal of American Ceramics Society*, **98**, 3956–3965.

Xie X., Yang H., Gu X. and Downs R.T. (2015) Chemical composition and crystal structure of merrillite from the Suizhou meteorite. *American Mineralogist*, **100**, 2753–2756.

Yamaguchi G., Ono Y., Kawamura S. and Soda Y. (1963) Synthesis of the modifications of Ca_2SiO_4 and determination of their powder X-ray diffraction patterns. *Journal of Ceramic Society of Japan*, **71**, 21–26.

Yang J.Y. and Oldroyd D. (2003) A Chinese palaeontologist, Ma Ting Ying (1899–1979): From coral growth-rings to global tectonics. *Epidodes*, **26**, 19–25.

Yashima M. and Sakai A. (2003) High-temperature neutron powder diffraction study of the structural phase transition between α and α' phases in tricalcium phosphate $Ca_3(PO_4)_2$. *Chemical Physics Letters*, **372**, 779–783.

Yashima M., Sakai A., Kamiyama T. and Hoshikawa A. (2003) Crystal structure analysis of β-tricalcium phosphate $Ca_3(PO_4)_2$ by neutron powder diffraction. *Journal of Solid State Chemistry*, **175**, 272–277.